# POLITECNICO DI TORINO

Corso di Laurea Magistrale in Ingegneria Aerospaziale

Tesi di Laurea Magistrale

# Analysis of $Mg$-$CO_2$ Rocket Propulsion for a Mars Ascent Vehicle exploiting in situ resources

Supervisors
Prof. ANDREA FERRERO
Prof. DARIO GIUSEPPE PASTRONE
Ing. FILIPPO MASSENI

Candidate

EMANUELE BARCA

July 2022

# Table of Contents

# List of Tables

# List of Figures

# Chapter 1

# Introduction

Human martian exploration is a long term International Space Exploration Coordination Group(ISECG)'s objective[1]. A key technology that would make possible to achieve this goal is In Situ Resources Utilization(ISRU). Typical ISRU proposals are based on propellants production by processing martian atmosphere. As measured by Viking landers[2], the lower martian atmosphere composition is as follows: $95.32\% CO_2$, $2.7\% N_2$, $1.7\% Ar$, $0.13\% O_2$ and lower percentages of other gases. ISRU concepts based on chemical processing, like producing methane and liquid $O_2$, have to choose between producing meaningful propellants quantities in short times with prohibitive surface power requirement or reducing the production rate leading to longer refueling times[3]. Seeing the abundance of $CO_2$ in the atmosphere, a simpler approach would be to use it directly as an oxidizer without the need of power costing chemical processing. This idea may seem counterintuitive, $CO_2$ being a typical combustion product, but some metals and their compounds can burn with it. Shafirovich[4] compared various metals and their hydrates as possible fuels and concluded that, even with a lower ideal Isp (see figure 1.2), magnesium is the most promising one, thanks to the ease of ignition in $CO_2$, the non-toxicity and the relative less condensed phase in combustion products as shown in figure 1.1. Viking landers[2] analyzed also martian regolith finding that 8.6% by mass consists of $MgO$, opening the opportunity to produce all the propellant, both the oxidizer and the fuel, in a future martian base. This opportunity led to the proposal and testing of two types of $Mg - CO_2$ rocket engines:

- A $Mg$ powder and liquid $CO_2$ one proposed by Shafirovich[5] and first tested by Wickman[6].

- An hybrid rocket engine with a paraffin wax-$Mg$ grain and a mixture of $CO_2 - N_2O$ as oxidizer, proposed and tested by Ozan Kara, Hakkı Karakaş and M. Arif Karabeyoğlu[7].

In addition to the decrease of mass to be transported from the Earth due to ISRU, these two types of engines offer the following advantages over traditional solid or liquid alternatives:

- Properties of $Mg$ powder and paraffin wax-$Mg$ grain are not influenced by Earth-Mars travel or by the low temperatures on martian surface.
- Fuel and oxidizer are not mixed like in a solid rocket motor grain, with the consequent benefit of managing two inert components.
- Ability of regulating and interrupting thrust.

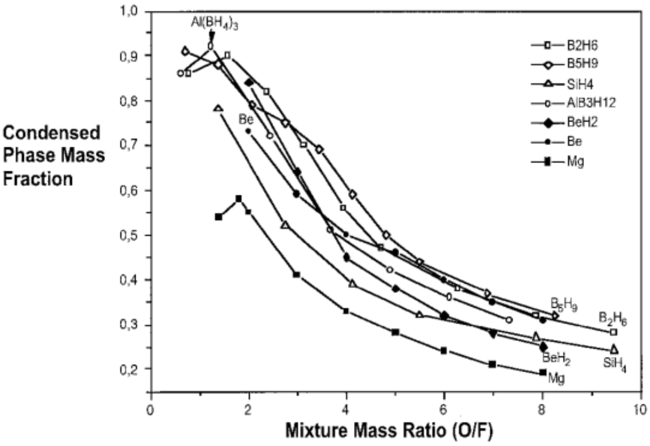

**Figure 1.1:** Mass fraction of condensed phase in a nozzle of a rocket using $CO_2$ as an oxidizer. Chamber pressure is 10 bar, exit pressure is 10 mbar[4]

In the following chapters a description of these two proposed engines is given. Next, supposing to apply them to a Mars Sample Return (MSR) mission, a simplified model predicting the mass fraction of payload to mass of the rocket sent from the Earth is used to compare their performances. Given the stages and propellants properties and the fractions of propellants eventually produced on Mars, the model permits to estimate the mass fractions of interest as functions of the oxidizer to fuel ratio and so to find the optimal one.

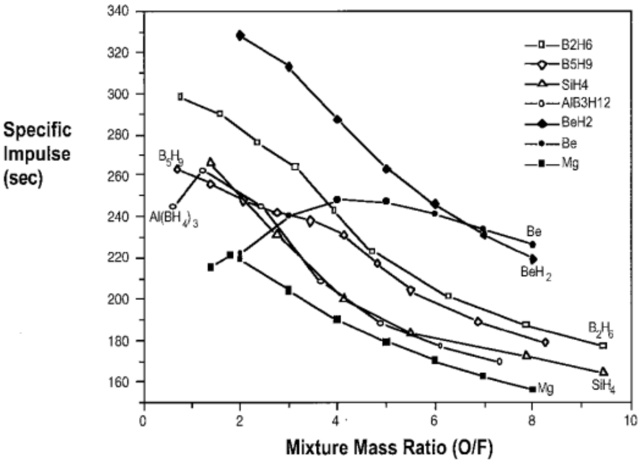

**Figure 1.2:** Ideal (without losses) specific impulse of a rocket using $CO_2$ as an oxidizer. Chamber pressure is 10 bar, exit pressure is 10 mbar[4]

# Chapter 2

# Powder $Mg - CO_2$ bipropellant engine

## 2.1 Research history

The use of a powder $Mg$-$CO_2$ engine for martian applications firstly proposed by Shafirovich[5], it's been the basis for subsequent research.

Wickman[6] tested a $Mg - CO_2$ rocket engine demonstrating its feasibility. However finding some problems like carbon deposition on the electrode ignition sources, making restarting less reliable. The $Mg$ powder feeding system consisted of pressurizing the fuel tank with nitrogen gas and, by controlling its flow, regulating the magnesium powder mass flow rate carried by the gas.

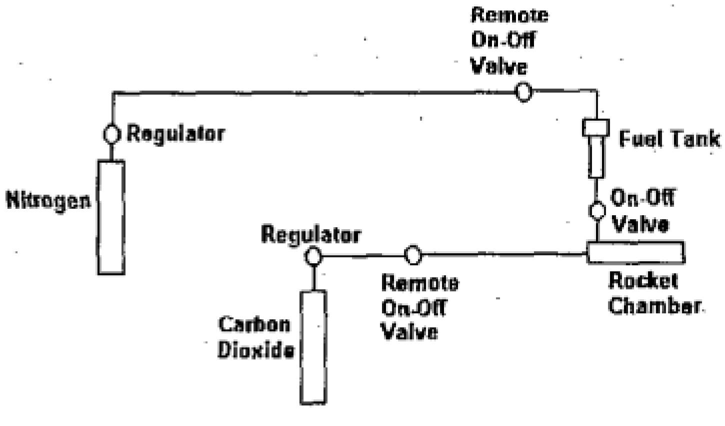

**Figure 2.1:** Wickman's[6] scheme of magnesium and carbon dioxide rocket engine feed system

A similar engine was tested also by Szabo[8], burning $Mg$ powder with $CO_2$, steam and hydrogen peroxide. Szabo found that measured Isp was around 70% of the theoretical predicted one for all the cases, despite the considerable differences in condensed combustion products fractions. From this observation, Szabo concluded that the engine worked with minimum two phase flow losses and attributed the low performance to non-adiabatic flow and non-optimal thrust chamber geometry.

Shafirovich[5] also noted that $Mg{-}CO_2$ combination is particularly advantageous over conventional storable propellants for missions involving multiple hops, like a MSR mission collecting samples from various martian regions. That's because between hops the oxidiser tank can be refilled and the only propellant to be brought from Earth is $Mg$ powder, drastically reducing mass and cost of the mission. This kind of mission will require the engine to deliver different thrust levels for flexible aircraft control, trajectory optimization, and energy management.

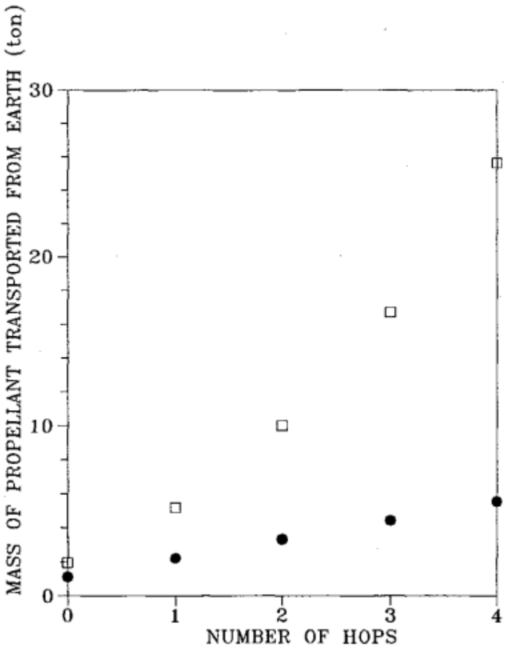

**Figure 2.2:** Mass of propellant transported from Earth vs the number of ballistic flights on Mars for engines on $N_2O_4{+}(CH_3)_2N_2H_2$(□) and $Mg{+}CO_2$ (●) propellants for 1 ton final mass (sum of structural mass and payload mass) brought to low Martian orbit after the hops[5]

Li[9][10] designed and tested a new powder feed system and combustion chamber with three gaseous $CO_2$ injections, demonstrating thrust modulation feasibility of this type of engine making it a good candidate for the martian hopper proposed by Shafirovich[5]. Following this work, Hu[11] studied the performance of such design using liquid $CO_2$ analyzing in detail the propellant feed, ignition, flame stabilization and combustion stability.

## 2.2 Engine description

The experimental rocket engine tested by Hu[11] has as its main components:

- liquid $CO_2$ tank;
- powdered $Mg$ tank/fuel feeder;
- high pressure $N_2$ tank to actuate the piston that pressurize the liquid $CO_2$ and acts as actuation gas in the fuel feeder;
- $CO_2$ evaporator that gasifies liquid $CO_2$ to be used for the fluidization of powder $Mg$;
- valves to control $CO_2$ and $Mg$ flow rate;
- plasma-jet igniter;
- thrust chamber.

Li's design[10] is different, using only high pressure $CO_2$ as oxidiser, actuation and fluidization gas.

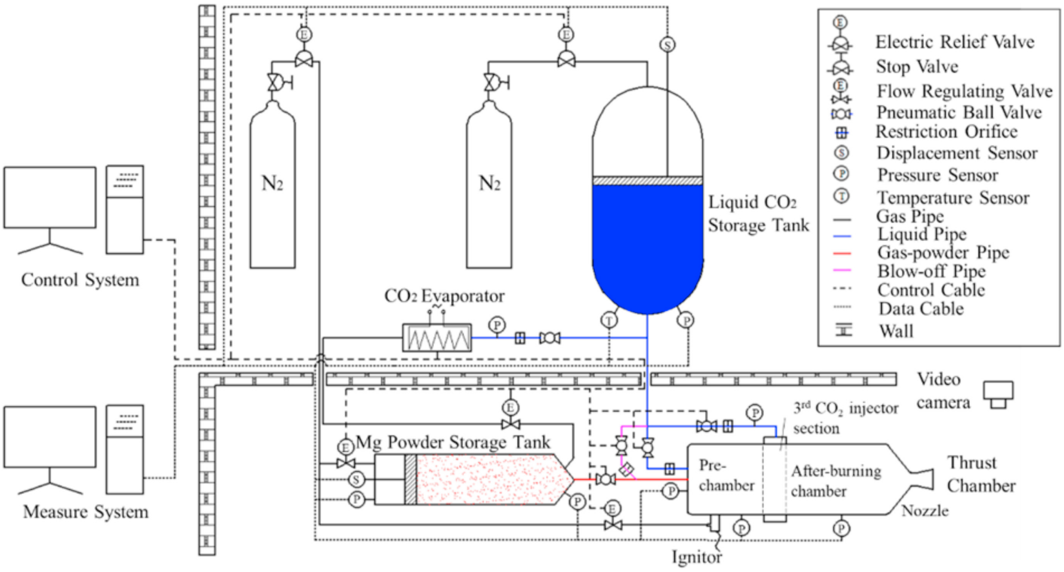

**Figure 2.3:** Hu's[11] experimental system of powdered $Mg$ and liquid $CO_2$ bipropellant rocket engine.

### 2.2.1 Fuel feeding system

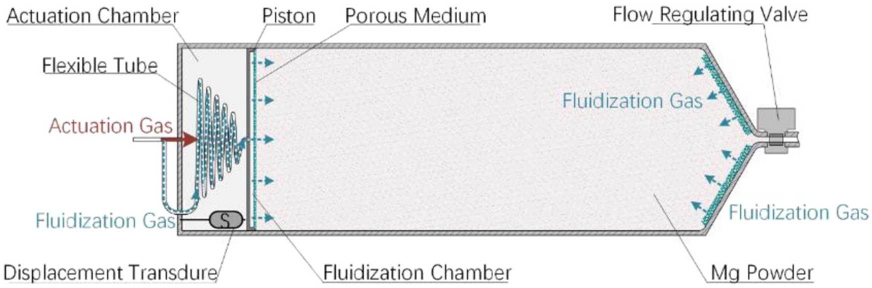

**Figure 2.4:** Fuel feeder[9]

$Mg$ powder is fed from a piston type expulsion tank. The tank is divided by the piston in fluidization chamber and actuation chamber. The actuation gas pressurizes the actuation chamber while the fluidization gas is injected into the fluidization chamber through a porous medium that prevents the passage of powder stored there. The fluidized powder is transported into the chamber in the form of suspension flow through a regulating valve that, varying the orifice area, makes possible to achieve fuel flow rate modulation. The fuel flow rate is well approximated by Eq.2.1[10].

$$\dot{m} = A_p \rho \frac{dS_p}{dt} \tag{2.1}$$

Where $\dot{m}$ is the powder mass flow rate, $\rho$ is the powder packing density, $A_p$ is the piston area and $\frac{dS_p}{dt}$ is the piston velocity.

During experimental tests Hu[11] verified that, even with chocking condition in the orifice, fluctuations occur in the fuel flow rate related to non-homogeneous gas-solid flow pattern. This is influenced by the solid phase volume fraction in the flow and by the slope of the powder feed pipe between the tank and the chamber [12].

### 2.2.2 Oxidizer feeding system

In Hu's work[11], liquid $CO_2$ is chosen over gaseous $CO_2$ due to the smaller size and therefore lower mass of the tank. The liquid $CO_2$ expelled from the tank by a piston actuated by high pressure $N_2$ is divided in four channels directing a part to the evaporator producing fluidizing gas, and the others to combustion chamber injectors. The total $CO_2$ flow rate follows the law defined by Eq. 2.1, where $\dot{m}$ is the total $CO_2$ flow rate, $\rho$ is the liquid $CO_2$ density, $A_p$ is the piston area and $\frac{dS_p}{dt}$ is the piston velocity. Due to low martian atmospheric pressure, ranging between

6.9 and 10 mbar [2], chamber pressure has to be limited to achieve low performance losses due to nozzle non-adaptation with relative low expansion ratio and as a consequence low nozzle mass. If chamber pressure is lower than the critical one, cavitation occurs in the feeding line, having the effect of reducing the injector's flow coefficient and so the liquid $CO_2$ flow rate passing through the orifice defined in Eq. 2.2.

$$\dot{m} = C_d A_{or} \sqrt{\rho \Delta p_{or}} \tag{2.2}$$

Where $\dot{m}$ is the liquid $CO_2$ flow rate passing through the orifice, $C_d$ is the flow coefficient, $A_{or}$ is the orifice area, $\rho$ is the liquid $CO_2$ density and $\Delta p_{or}$ is the difference between the pressure upstream of the injector and the pressure downstream, equal to the chamber pressure.

### 2.2.3 Combustion chamber

The first $Mg - CO_2$ rocket engine tested by Wickman[6] used a simple cylindrical chamber with a single $Mg$ powder injector and a single gaseous $CO_2$ injector as seen in figure 2.5.

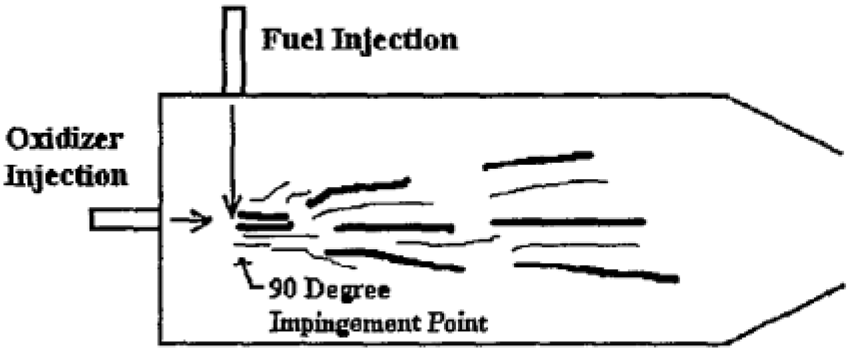

**Figure 2.5:** Rocket chamber cross-section and injectors scheme[6]

The $CO_2$ and $Mg$ powder were respectively injected axially and radially. $CO_2$ was injected as a high velocity jet to "atomize" the powder. Even with such a simple injection scheme the engine reached levels of combustion efficiencies, defined in Eq.2.4, as high as 87%.

$$c^* = \frac{p_c A_t}{\dot{m}} \tag{2.3}$$

$$\eta_{comb} = \frac{c^*_{exp}}{c^*_{th}} \tag{2.4}$$

Where $c^*_{exp}$ is the experimental characteristic exhaust velocity and $c^*_{th}$ is the theoretical one.

Li[10] analyzed more in detail the combustion characteristics of powder $Mg$ and gaseous $CO_2$ designing a new combustion chamber with three injection zones, displayed in figure 2.6. The multiple $CO_2$ injection zones are meant to control the local and global oxidizer to fuel ratio. A similar combustion chamber was also tested by Hu[11], using liquid $CO_2$ instead.

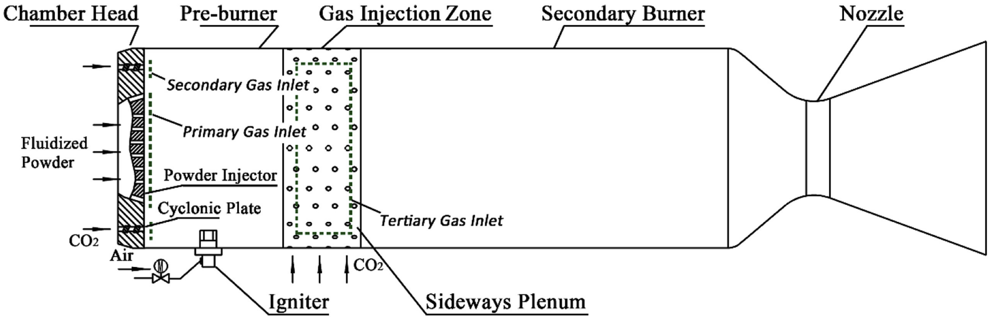

**Figure 2.6:** Li's thrust chamber[10]

The fluidized $Mg$ powder, with diameters smaller than 100 $\mu$m, injected in the chamber head behaves like a fluid and the combustion process is similar to that of liquid rockets[10]. Legrand[13] found that the burning time law of $Mg$ particles, with diameters ranging from 50 $\mu$m to 2.5 mm, in $CO_2$ is well approximated by Eq. 2.5.

$$t_b = K d_0^2 \tag{2.5}$$

Where $d_0$ is the starting diameter and $K = 0.5\ s/mm^2$ is an empirical constant.

During chamber design, Li assumed an ignition temperature of 1100 K, mean environment temperature of 1500 K (half of the adiabatic flame temperature) and 60 $\mu$m diameter particles, estimating a burning time of 1.8 ms by Eq.2.5 and an ignition time of 8.5 ms by heat conduction calculation. Adding these two times values the minimum chamber permanence time is found. Li obtained a theoretical chamber length of 150 mm multiplying the minimum chamber permanence time to an assumed average flow velocity of 15 m/s. In addition an amplification coefficient of 2 was used to account for different flow regimes, obtaining a chamber with the parameters reported in table 2.1.

| | | |
|---|---|---|
| Particle Parameters | Postulated Diameter | 60 $\mu$m |
| | Ignition Time | 8.5 ms |
| | Burn Time | 1.8 ms |
| | Average Injection Velocity | 5 m/s |
| Operating Parameters | Chamber Pressure | 1.0 MPa |
| | Powder Flow Rate | 5-50 g/s |
| | O/F Ratio | 2-6 |
| | Average Flow Velocity | 15 m/s |
| Chamber Parameters | Chamber Length | 300 mm |
| | Chamber Diameter | 50 mm |
| | Throat Diameter | 8 mm |

**Table 2.1:** Li's combustion chamber design parameters[10]

As can be seen in figure 2.6, the combustion chamber is divided in a pre-burner and a secondary burner. In the pre-burner a fuel rich mixture, needed to a stable combustion [10], is obtained by:

- injecting the fluidized $Mg$ axially with the primary $CO_2$ gas and dispersing it into the burner by a porous bluff-body installed at the injector's outlet;
- injecting the secondary $CO_2$ gas with an annular injector in the chamber head which imposes a tangential component to the gas velocity favoring mixing.

After the pre-burner the injection of tertiary $CO_2$ gas takes place in order to reach the wanted global mixture ratio.

### 2.2.4 Ignition

In Li's engine[10], which uses gaseous $CO_2$, an air flow is injected into the pre-burner through two annular electrodes. Such flow, once ionized, ignites the two-phase flow with the resulting plasma. In Hu's engine[11], which uses liquid $CO_2$, the plasma igniter is insufficient to ignite the three phase mixture (the solid $Mg$, the primary gaseous $CO_2$ and the secondary and tertiary liquid $CO_2$), due to the additional energy required to vaporize the liquid droplets. To get around this problem, a multi stage ignition is used, igniting first the primary gas and $Mg$ powder and then, once achieved a stable flame, the secondary and tertiary liquid $CO_2$ are injected.

With his liquid $CO_2$ engine[11] tests, Hu concluded that in order to achieve a successful ignition, with the stage ignition procedure described above, it's sufficient to have a Damköhler number (defined in Eq.2.6) higher than 1 in the pre-burner.

$$Da = \frac{t_s}{t_{ch}} = \frac{L}{u_{inj}(t_i + t_b)} \tag{2.6}$$

$$t_i = A \ln\left(1 + \frac{C}{T_A - B}\right) \tag{2.7}$$

Where $t_s = \frac{L}{u_{inj}}$ is the permanence time of the particle in the pre-burner, L is the pre-burner length, $u_{inj}$ is the average powder injection velocity and $t_{ch} = t_i + t_b$ is the chemical reaction time. The ignition delay time $t_i$ is dependant on ambient temperature $T_A$ and particle size (A,B,C in Eq.2.7 are empirical constants for the particle size selected) while the burning time $t_b$ is defined in Eq.2.5.

Li tested the ignition capability and the influence of primary and secondary gas flow rate ratio, finding from ignition test results a boundary function delimiting ignition success and failure. Besides the boundary function Li defined three constraints:

- Flame propagation condition: the fluidization gas and particle velocity in the transport duct should be higher than the $Mg - CO_2$ flame propagation velocity ($1.0 \pm 0.1\ m/s$)[8][10].
- Primary gas flow rate limitation: the higher the particle speed is, the shorter the residence time will be in the igniter flame, limiting particle velocity to successful ignition[10].
- Secondary gas flow rate limitation: if the secondary gas velocity is too high it can destroy the igniter flame structure[10].

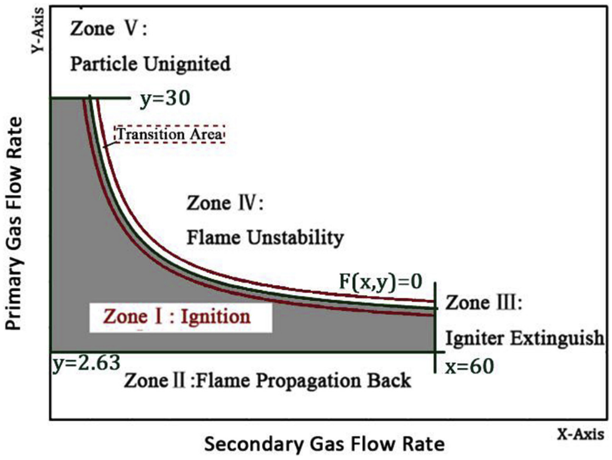

**Figure 2.7:** Li's empirical model for ignition feasibility in $Mg - CO_2$ powder rocket engine with a 400 W plasma igniter.[10]

Figure 2.7 displays the five zones defined by Li's empirical model of ignition:

- Zone I: in this zone the primary and secondary flow rates permit a successful ignition.
- Zone II: in this zone the ignition is possible but the flame propagates with a higher speed than that of particles and primary gas, with a consequent propagation back of the flame.
- Zone III: the secondary gas flow rate is too high and destroys the igniter flame.
- Zone IV: points in this zone are above the boundary function leading to a failed ignition.
- Zone V: the primary gas flow rate is too high and the particle permanence time in the ignition zone is too small to ignite.

### 2.2.5 Combustion

In the combustion chamber two chemical reactions take place simultaneously: the gas-phase reaction (see Eq.2.8) and the heterogeneous reaction (see Eq.2.9).

$$Mg + CO_2 \rightleftharpoons MgO(s) + CO \tag{2.8}$$

$$Mg(l) + CO \rightleftharpoons MgO(s) + C(s) \tag{2.9}$$

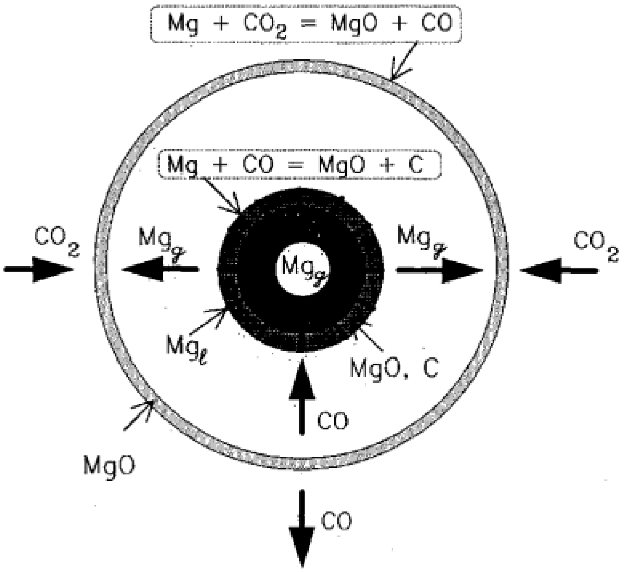

**Figure 2.8:** Schematic representation of Mg particle combustion in $CO_2$[5]

These two reactions take place around the $Mg$ particles in two separated areas, as schematized in figure 2.8. The heterogeneous reaction can take place in an environment with temperature lower than 2000 K, limiting it near or on the liquid particle surface ($Mg$ melts and boils at 923 K and 1100 K, respectively). The heterogeneous reaction taking place on the particle surface produces a solid shell of carbon and $MgO$ which is broken by the pressure of the vaporizing liquid metal inside it, making possible the complete combustion of the $Mg$ particle[5]. If the chamber concentration of $CO$ is less than 25%, gas phase reaction is the dominating one and there is stable combustion with an higher burning rate[5].

To evaluate the influence of the different parameters to the combustion characteristics, Li carried out a series of firing tests divided into four groups[10]:

1. **Injection effect of secondary gas and tertiary gas**. The primary gas flow rate is kept constant varying the secondary and tertiary flow rates;
2. **Variation of local O/F ratio in chamber head**. The primary gas flow rate and the sum of the secondary and tertiary flow rates are kept constant, varying the ratio between the secondary and tertiary and as a consequence the O/F in the chamber head;
3. **Fraction variation of fluidization gas in chamber head**. The sum of primary and secondary gas flow rates and the tertiary flow rate are kept constant, varying the primary and secondary gas flow rates ratio;
4. **Global O/F ratio effect**. The three flow rates are varied to obtain different global O/F with a head O/F value half of the global one.

Li evaluated the performance variations in the various tests using the definitions of combustion efficiency in Eq.2.4 and characteristic velocity in Eq.2.3, averaging the chamber pressure value as defined in Eq.2.12 and defining the minimum and maximum values reached by the chamber pressure in its oscillation in Eq.2.10-2.11.

$$p_{min} = \left| \int_t^{t+1} p\left(t\right) dt \right|_{min} ; \quad t \in \left(t_{ign}, t_{ter}\right) \tag{2.10}$$

$$p_{max} = \left| \int_t^{t+1} p\left(t\right) dt \right|_{max} ; \quad t \in \left(t_{ign}, t_{ter}\right) \tag{2.11}$$

$$\overline{p_c} = \frac{\int_{t_a}^{t_b} p\left(t\right) dt}{t_b - t_a} \tag{2.12}$$

Where $p\left(t\right)$ is the chamber pressure, $t_a$ is the time value at which the pressure reaches the 70% of $p_{max}$ for the first time and $t_b$ is the time during the shut-off when the pressure drops below 70% of $p_{max}$[10].

### Injection effects of secondary and tertiary gas

From the first set of tests, Li concluded that increasing the secondary gas flow rate decreases the efficiency but stabilizes the flame, while the tertiary gas flow rate has the opposite behavior. In figure 2.9 these effects can be seen in the reported tests results injecting only the secondary or tertiary gas in addition to the primary one. The dots represent the average efficiency and the bars the deviation due to pressure oscillation. The fact that the efficiency is lower when only the tertiary gas is injected indicates that the secondary gas mixing contribution and chamber head O/F are important to the combustion efficiency.

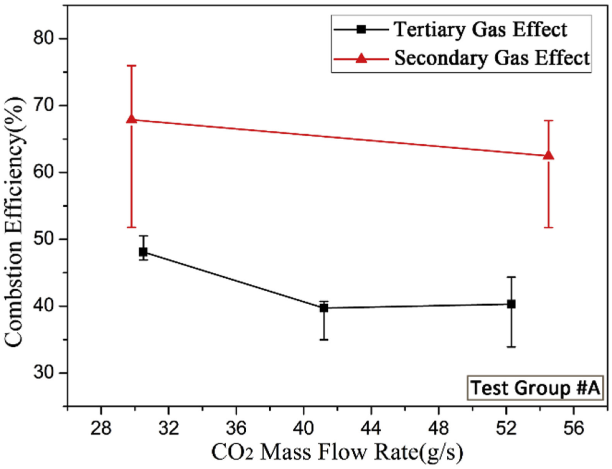

**Figure 2.9:** Effects of gas injection way[10]

### Variation of local O/F ratio in chamber head

From the second set of tests, one can observe a combination of the behaviors seen with the injection of only one between the secondary and tertiary gas flow rates. The increase of chamber head O/F from minimum secondary flow rate to the maximum secondary flow rate leads to an increase in efficiency and instability as shown in figure 2.10. Such behavior might have been expected from intermediate situations to the extremes ones (with only the tertiary or secondary flow injection) analyzed in the previous set of tests. The deposition of magnesium oxide and carbon is located mainly in the chamber head and near the third injection zone[10]. The heterogeneous reaction is promoted by the fuel rich environment and low secondary gas temperature near the wall in the pre-burner, and by the low temperature of the tertiary gas in its injection zone. Li[10] noted, studying the variation of deposition in chamber head with respect of its O/F, that to the increase of O/F and efficiency is associated a decrease of the heterogeneous reaction and as a consequence of deposition.

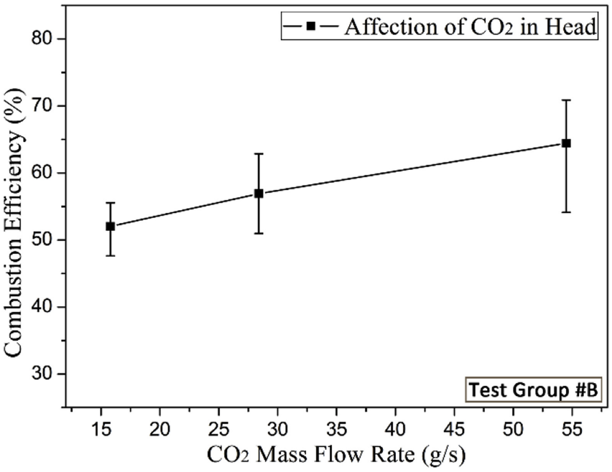

**Figure 2.10:** Effects of $CO_2$ flow rate in the chamber head and consequently of local O/F variation [10]

### Fraction variation of fluidization gas in chamber head

The variation of the fraction of fluidization gas flow rate in combustion chamber head seems to influence the efficiency in a non-monotone way, firstly increasing then decreasing it as shown in figure 2.11, meaning that there is an optimum fluidization O/F. Li[10] explained this trend noting the similar deposition behaviour when the fluidization gas flow rate is increased:

- first a reduction of deposition, due to the increase of O/F of the fuel rich chamber head environment;
- then an increase of deposition due to the increased injection speed of the particle which easily reaches the coldest wall area.

### Global O/F ratio effect

O/F influences the chamber temperature and the concentration of chemical species as shown in figure 2.12 and 2.13. Moreover, temperature and concentration of $CO$ directly affect the type of reaction taking place and the presence of carbon deposits, as analyzed in the previous paragraphs. The changes in temperature influence also the heat transfer. During the tests, Li[10] measured the heat loss of his test engine for several O/F, finding that performance losses decreased increasing the O/F and were around the 3%.

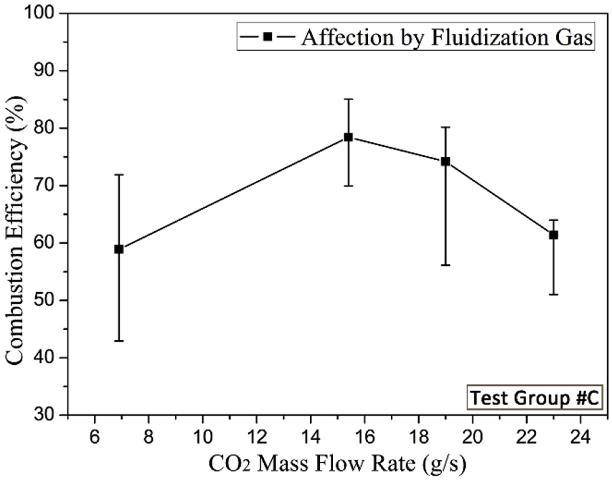

**Figure 2.11:** Effect of fluidization gas flow rate fraction in chamber head[10]

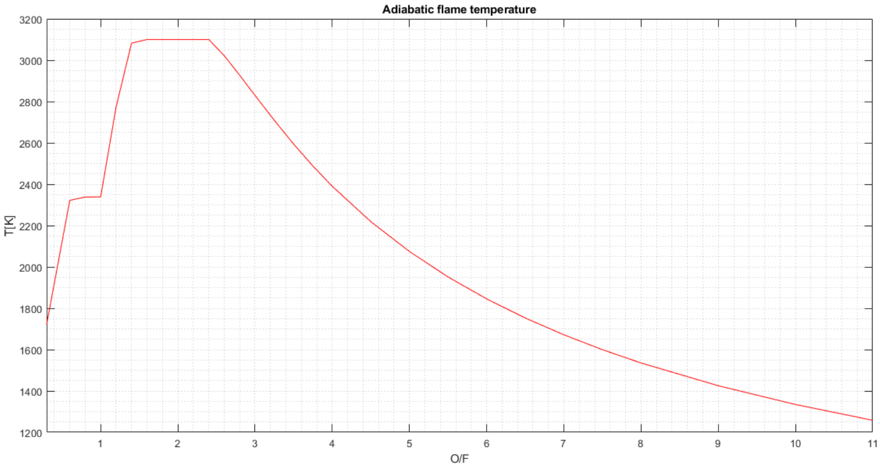

**Figure 2.12:** Adiabatic flame temperature for $Mg$-$CO_2$ with $p_c = 1$ MPa from CEA[14][15] analysis

### 2.2.6 Combustion pressure oscillation

Gaseous and liquid $Mg - CO_2$ rocket engines are characterized by low frequency pressure fluctuations [10][11]. Analyzing the pressure data in the frequency domain by Fourier transformation, Li observed that the dominant frequencies are related to the fluidization gas and the secondary gas. Hu related the pressure fluctuations to the $Mg$ feeding piston movements and deposition near the oxidizer nozzles, suggesting that a smoother powder feeder and a reduction of deposition could possibly improve engine stability.

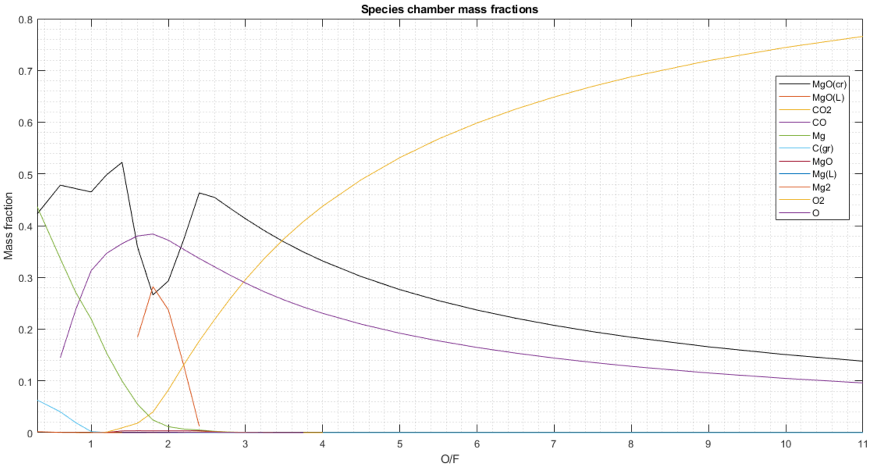

**Figure 2.13:** Chemical species mass fractions for $Mg$-$CO_2$ with $p_c = 1$ MPa from CEA[14][15] analysis

# Chapter 3

# Paraffin wax-$Mg/CO_2$-$N_2O$ hybrid rocket motor

Ozan Kara and Arif Karabeyoglu[16] proposed and tested a classical hybrid rocket motor configuration using a heavy metallic loaded paraffin wax grain and $CO_2/N_2O$ mixture as oxidizer, putting together ISRU, the advantages of not needing a fuel feeding system and the paraffin relative high regression rate.

## 3.1 Hybrid rocket motor fundamentals

In hybrid rocket motors propellant is stored in two different states: liquid and solid. The classical configuration consists of a solid fuel grain and a liquid oxidizer. The separation of fuel and oxidizer typical of liquid engines and the presence of a solid fuel grain in the combustion chamber similar to the solid rocket motors, give to this design the following advantages[17]:

- Safety: unlike in the solid motors, the solid grain is inert and can be stored and handled more simply needing an external oxidizer to burn.
- Throttling, shutdown and restart: varying the liquid flow rate is possible to vary the thrust, shut down and restart the system. These capabilities make it more safe and flexible than solid rocket motors, permitting an abort procedure in the case of failure and the possibility of multiple burns during the mission.
- Grain robustness: fuel grain cracks are not catastrophic like in solid fuel motors because combustion occurs in the boundary layer where, by diffusion, fuel and oxidizer mix, and not directly on the surface.
- Low temperature sensitivity: the regression rate is almost not influenced by grain initial temperature, so the hybrid rocked motor is assumed to work with

the same performance with different ambient temperatures unlike the solid motor.

- No need for a fuel feeding system and tank: like in solid rocket motors the combustion chamber also has the role of fuel tank, simplifying the design.

These advantages come with some disadvantages:

- Low regression rate: the hybrid solid grains have lower regression rates compared to solid ones. This can lead to multiple port configuration to achieve the same thrust levels.
- Low bulk density: As a consequence of a multiple port configuration and the need of an area for injection in chamber head and one for mixing after the grain, the fuel volume fraction in the combustion chamber is lower than that of an equivalent solid motor. This leads to hybrids with larger envelope for a given mission.
- Combustion efficiency: Due to the combustion process governed by diffusion, there is a lower degree of mixing than in liquids and solids, with greater specific impulse losses.
- OF shifting: The port area becomes bigger during the burn, varying the regression rate and OF, possibly lowering theoretical performance.

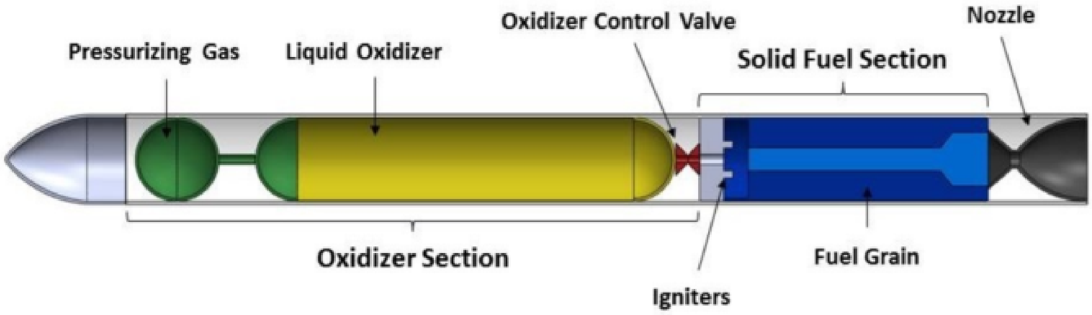

**Figure 3.1:** Typical hybrid rocket configuration[16]

### 3.1.1 Hybrid rocket motor interior ballistic: classical hybrid combustion theory

One characterizing parameter of hybrid rocket motors is the regression rate, this section summarizes the models used to estimate it for classical hybrid propellants.

In the hybrid's combustion chamber, the vaporized liquid injected in the chamber head passes through the port area forming a boundary layer on the grain surface and reacting with it. Due to the separation of fuel and oxidizer, the combustion takes place not directly on the surface like in solid motors but in the boundary layer above it, where an adequate mixture ratio is reached. Marxman and Gilbert[18] modelled the combustion zone as in figure 3.2, where the boundary layer is divided in a fuel rich and an oxidizer rich zone by the flame, considered of negligible thickness and positioned at a distance from the surface where the concentrations of reactants are sufficient for combustion to take place. Marxman and Gilbert[18] hypothesized that the heat transfer from the flame to the fuel surface was the controlling mechanism of hybrid combustion, and by an energy flux balance on the fuel surface obtained an expression for the regression rate[18][19]:

$$\rho_s r \Delta H_{v,eff} = Q_{tot} \tag{3.1}$$

Where $\rho_s$ is the solid fuel density, r is the regression rate, $Q_{tot}$ is the heat flux absorbed by fuel surface and $\Delta H_{v,eff}$ is the effective heat of gasification of the fuel. From this equation, assuming[19]:

- turbulent boundary layer flow on all the surface due to the destabilizing effect of blowing;
- the Reynolds analogy is valid in the zone below and above the flame sheet but not necessary in the flame itself, meaning that the energy and momentum transport in these zones are similar;
- Lewis number, defined as the ratio of thermal diffusivity to mass diffusivity, and Prantl number, defined as the ratio of momentum diffusivity to thermal diffusivity, are equals to unity in the zone below and above the flame sheet but not necessary in the flame itself;
- The velocity profile in the boundary layer is not affected by blowing and by the flame, and the standard friction coefficient for turbulent boundary layer remains the same;
- The main contribution to heat transfer is convection;

Marxman and Gilbert[18] obtained:

$$\rho_s r = CGRe_x^{-0.2} \frac{St}{St_o} \frac{u_e}{u_{fl}} \frac{(h_{fl} - h_w)}{\Delta H_{v,eff}} \tag{3.2}$$

$$\rho_s r_{rad} = \sigma \epsilon_w \frac{\left(\epsilon_g T_g^4 - \alpha_g T_w^4\right)}{\Delta H_{v,eff}} \tag{3.3}$$

Adding 3.3 to the right side of eq.3.2 to take account of the radiant heat. Where $C$ is a function of the mainstream Mach number, $G$ is the total mass flux, $St$ is the Stanton number defined in eq. 3.4 and $St_o$ is the Stanton number without blowing for turbulent flow over a flat plate, $u_e$ and $u_{fl}$ are respectively the velocity at the edge of the boundary layer and at the flame, $h_{fl}$ and $h_w$ the total enthalpy at the flame and at the wall of the gas phase, $\Delta H_{v,eff}$ is the heat of gasification and $Q_{tot}$ is the total heat flux to the surface as in eq. 3.1, $\sigma$ is the Stephan-Boltzmann constant, $\epsilon_w$, $\epsilon_g$ and $\alpha_g$ are respectively the emissivity of the surface and gas and absorptivity of the gas, $T_g$ and $T_w$ are the gas and surface temperature.[19]

$$St = \frac{Q_{tot}}{\rho_e u_e \left(h_{fl} - h_w\right)} \tag{3.4}$$

The reduction of heat transfer caused by blowing, accounted by the Stanton number ratio, increase with the blowing itself leading to a "blockage" effect that limits the regression rate.

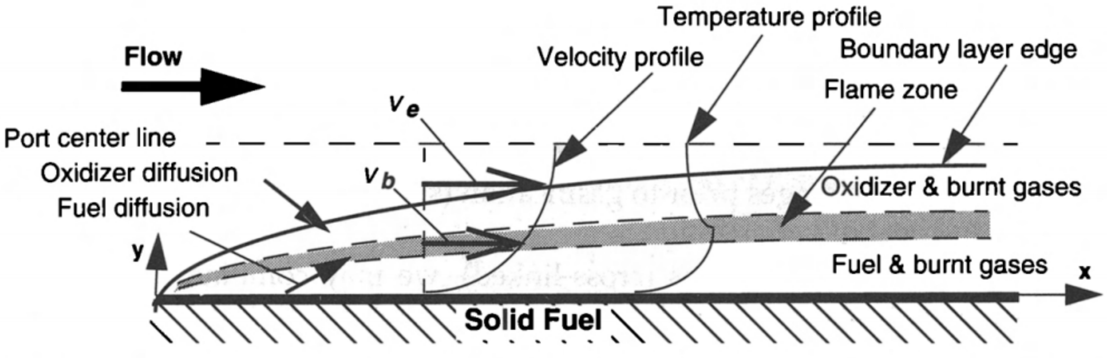

**Figure 3.2:** Schematic of combustion zone above hybrid fuel[17]

Marxman and Gilbert[18] approximated the Stanton numbers ratio in eq.3.6, as a function of the mass transfer parameter B, defined in eq.3.5 [19]:

$$B = \frac{\rho_s r}{\rho_e u_e \frac{C_f}{2}} = \frac{u_e}{u_{fl}} \frac{\left(h_{fl} - h_w\right)}{\Delta H_{v,eff}} \tag{3.5}$$

$$\frac{St}{St_o} = 1.2 B^{-0.77} \quad for \quad 5 < B < 100 \tag{3.6}$$

Velocity ratio between the flame and boundary layer edge is found by Marxman and Gilbert[18] to be a function of the propellant combination properties (Eq.3.7)[19].

$$\frac{u_{fl}}{u_e} = \frac{\left[O/F_f \frac{\left(h_{fl}-h_w\right)}{\Delta H_{v,eff}}\right]}{K_{OX_e} + \left(O/F_f + K_{OX_e}\right)\left[\frac{\left(h_{fl}-h_w\right)}{\Delta H_{v,eff}}\right]} \tag{3.7}$$

Where $K_{OX_e}$ is mass fraction of the oxidizer at the edge of the boundary layer and $O/F_f$ is the oxidizer to fuel ratio at the flame. Substituting the definition of B and the approximation of the Stanton numbers ratio in eq.3.2 and expliciting the $Re_x$, a simplified regression rate expression for hybrid combustion with no radiant heat transfer is found[19]:

$$\rho_f r \propto B^{0.23} G^{0.8} x^{-0.2} \tag{3.8}$$

The relation 3.8 clearly shows the dependency of the regression rate on the axial position with the decreasing term $x^{-0.2}$, but depends on it even with the flow rate flux $G$ that, being the sum of the constant oxidizer flow rate flux passing through the port area and the fuel flow rate flux increasing along the grain axis, increases with $x$. Due to these two opposing trends, the regression rate tends to be almost constant along the axis length[17]. Fixed the propellant combination, $B$ is almost fixed, depending only on propellant properties, and can be considered constant. With these considerations, an averaged regression rate can be easily expressed starting from 3.8:

$$r = aG_o^n \tag{3.9}$$

Where $G_o$ is the oxidizer flow rate flux through the port area and $a$ and $n$ are empirical constants. In the case of combined convective and radiant heat transfer, Marxman showed that the regression rate can be estimated from[20]:

$$\rho_s r = \frac{\left[ Q_c e^{\left( -\frac{Q_{rad}}{Q_c} \right)} + Q_{rad} \right]}{\Delta H_{v,eff}} \tag{3.10}$$

Where $Q_c$ is the convective heat flux in the case of no radiation and $Q_{rad}$ is the radiant heat flux defined in 3.11. As can be seen there is a counteracting effect that limits the contribution of an increasing radiant heat flux, decreasing the convective one, limiting the beneficial contribution of radiation.

$$Q_{rad} = \sigma \epsilon_w \left( \epsilon_g T_g^4 - \alpha_g T_w^4 \right) \tag{3.11}$$

### 3.1.2 Hybrid rocket motor interior ballistic: liquefying solid fuels

Experiments on cryogenic fuels and paraffin grains demonstrated an extraordinary increase in regression rate compared with that of traditional hybrid fuels like hydroxyl-terminated polybutadiene(HTPB). Karabeyoglu[21] produced a regression rate theory for liquefying solid fuels, like cryogenic fuels an paraffin, adding the entrainment (figure 3.3) fuel mass transfer mechanism to the Marxman model. Due to high chamber temperature a molten layer is formed on the solid grain surface, the high velocity gas flowing through the port area destabilizes it producing droplets that are carried away from the surface. This additional fuel mass transfer does not contribute to blowing and therefore is not affected by and does not trigger the blockage effect that limits the regression rate.

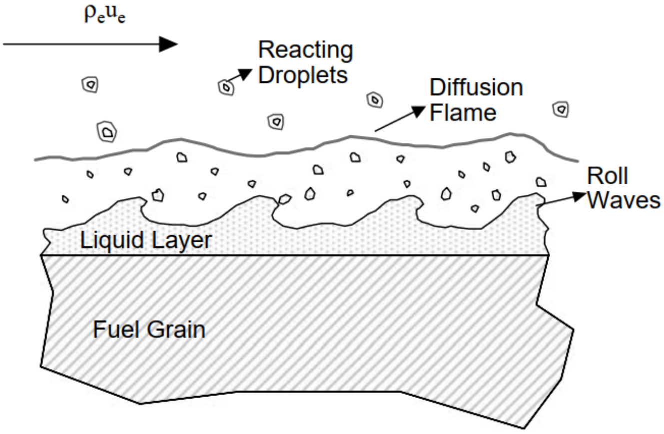

**Figure 3.3:** Karabeyoglu's schematic of entrainment process in hybrid rocket combustion[19]

To include the entrainment mechanism in the classical hybrid combustion theory, Karabeyoglu[21] made three major modifications:

- the ratio $\frac{(h_{fl}-h_w)}{\Delta H_{v,eff}}$ in the definition of the blowing parameter is different because the heat of gasification is reduced by the fraction of mass leaving the surface due to entrainment that only needs to be liquefied, and because the enthalpy difference between the flame and the surface is reduced, some reactants being in liquid form. Karabeyoglu assumed the last variation is negligible compared to the first one;

- the blocking factor $\frac{St}{St_o}$, is only dependant by the evaporation blowing parameter and the droplets evaporate and react only above the flame sheet;

- the ripples formed on the liquid surface increase the surface roughness and heat transfer.

By estimating firstly the liquid layer thickness by thermal analysis, then the stability of it under the shear of gas flow and linking it to the entrainment of liquid droplets with semi-empirical relations and experimental data, Karabeyoglu[21] has come to describe the hybrid combustion of liquefying solid fuel with a set of nonlinear algebraic equations that can be solved to obtain the regression rate for a given propellant in function of the axial position and the local flow in the port[21]. The modelling equations are the following:

$$r = r_v + r_{ent} \tag{3.12}$$

Where $r$ is the total regression rate, sum of the vaporization/gasification one $r_v$, and that caused by entrainment $r_{ent}$.

$$r_v + \left[R_{he} + R_{hv}\left(\frac{r_v}{r}\right)\right] r_{ent} = F_r \frac{0.03\mu_g^{0.2}}{\rho_s}\left(1 + \frac{Q_r}{Q_c}\right) B \frac{St}{St_o} G^{0.8} x^{-0.2} \tag{3.13}$$

Equation 3.13 represents the energy balance at gas-liquid interface. $R_{hv}$, and $R_{he}$ defined in 3.14 are the vaporization and the entrainment non dimensional energy parameters. $R_{hv}$ is the ratio between the heat required to bring the liquid layer from melting temperature $T_m$ to vaporization temperature $T_v$ ($C_l$ is the specific heat of the liquid, $\Delta T_1 = T_v - T_m$), and the total effective heat of gasification, being $h_e = h_m + C_l \Delta T_l$ the total heat of entrainment and $L_v$ the latent heat of vaporization. $R_{he}$ is the ratio between the total heat of melting $h_m$ and the total heat of gasification. The term in square brackets represents the assumption that the effective heat necessary to the fuel flow rate going through the entrainment mechanism decreases linearly as the vaporization component of the regression rate decreases[22]. $Fr$ is the roughness parameter taking account of the different heat transmission of the rippled surface.

$$R_{hv} = \frac{C_l \Delta T_l}{h_e + L_v}; \quad R_{he} = \frac{h_m}{h_e + L_v} \tag{3.14}$$

$$F_r = 1 + \frac{14.1\rho_g^{0.4}}{G^{0.8}\left(\frac{T_g}{T_v}\right)^{0.2}} \tag{3.15}$$

$$r_{ent} = a_{ent} \frac{G^{2\alpha}}{r^{\beta}} \tag{3.16}$$

$$a_{ent} = K \frac{C_f a_t^{\beta} \rho_l}{\mu_l \rho_s} \tag{3.17}$$

The regression rate due to entrainment is represented by Eq.3.16, where $a_{ent}$ is the entrainment coefficient defined in eq.3.17, dependent on propellant and liquid layer properties and assumed constant for a given propellant, $\alpha$ and $\beta$ are empirical constants. $a_t$ in the definition of $a_{ent}$ is the thickness parameter, dependant on fuel properties and fraction of radiative heat over the total heat[23].

$$\frac{St}{St_o} = \frac{2}{2 + 1.25B_g^{0.75}} = \frac{C_{B1}}{C_{B1} + C_{B2}\left(\frac{r_v}{r_{cl}}\right)^{0.75}} \tag{3.18}$$

In the case of liquefying solid fuels the blocking factor represented by the ratio of Stanton numbers is approximated by Eq.3.18 and not by Eq.3.6 that leads to unrealistic values grater than unity for B<1. In eq.3.18 appears the classical regression rate, defined with the use of one of the coefficients in 3.19.

$$C_{B1} = \frac{2}{2+1.25B^{0.75}}; \quad C_{B2} = \frac{1.25B^{0.75}}{2+1.25B^{0.75}} \tag{3.19}$$

$$r_{cl} = \frac{0.03\mu_g^{0.2}}{\rho_s}\left(1+\frac{Q_r}{Q_c}\right)BC_{B1}G^{0.8}x^{-0.2} \tag{3.20}$$

Iteratively solving the set of equations 3.12, 3.13, 3.14, 3.15, 3.16, 3.18, Karabeyoglu was able to predict the regression rate laws for various propellants with a reasonable accuracy[22]. In [23] the theory has been improved, normalizing the equations by the classical regression rate and deriving a non-dimensional universal regression rate law, successfully tested with experimental data on a series of normal alkanes($C_2H_{2n+2}$) fuels. The equations become:

$$\phi = \phi_v + \phi_{ent}; \tag{3.21}$$

$$\phi_v + \left[R_{he} + R_{hv}\left(\frac{\phi_v}{\phi}\right)\right]\phi_{ent} = \frac{Fr}{C_{B1}+C_{B2}\phi_v}; \tag{3.22}$$

$$\phi_{ent} = \frac{R_{ent}}{\phi^{\beta}} \tag{3.23}$$

$$\phi = \frac{r}{r_{cl}}; \quad \phi_v = \frac{r_v}{r_{cl}}; \quad \phi_{ent} = \frac{r_{ent}}{r_{cl}}; \quad R_{ent} = a_{ent}\frac{G^{2\alpha}}{r_{cl}^{\beta+1}} \tag{3.24}$$

Where $R_{ent}$ is the entrainment parameter. Karabeyoglu solved the system ignoring the surface roughness (Fr=1), for $R_{ent}$ values between 0 and 300 and assigning constant values to B, $R_{he}$, $R_{hv}$ and $\beta$, finding that the non-dimensional total regression rate is well fitted by an equation of the following form[23]:

$$\phi = 1 + AR_{ent}^{C} \tag{3.25}$$

Choosing $\beta = 2$,the constants are C=0.4 and A=0.61. Karabeyoglu[23] noted that variations of B, $R_{he}$, $R_{hv}$ have small effect on the total regression rate, concluding that the equation 3.25 can be treated as an universal regression rate law for the chosen $\beta$. From eq.3.21 and 3.22 can be seen that when there is only entrainment $R_{ent} \to \infty \to \phi_v = 0 \to \phi = \phi_{ent} = \frac{Fr}{C_{B1}}$, so eq.3.25 has an asymptote. The entrainment parameter $R_{ent}$ can be written as[23]:

$$R_{ent} = K\frac{a_t^{\beta}\rho_s^{\beta}\rho_l}{\mu_l}C_{B1}^{-\beta}B^{-(\beta+1)}\left(1+\frac{Q_r}{Q_c}\right)^{-(\beta+1)}G^{2\alpha-0.8\beta-1}x^{0.2\beta} \tag{3.26}$$

From Eq.3.26 can be seen that $R_{ent}$ is a strong function of fuel properties (mostly the solid fuel density), of the blowing parameter and heat ratio, and a weak function of the local flux and axial position. The blowing parameter can be estimated combining Eq.3.5 and 3.7 as a function of oxidizer to fuel ratio of combustion and mass fraction of oxidizer at the boundary layer's edge.

$$B = \frac{K_{OX_e} + \left(O/F_f + K_{OX_e}\right)\frac{\left(h_{fl}-h_w\right)}{\Delta H_{v,eff}}}{O/F_f} \tag{3.27}$$

Knowing the propellant combination properties and the heat ratio, is possible to evaluate B and $r_{cl}$ and determining $\alpha$, $\beta$ and $K$ from experimental data fitting, it is possible to estimate the total regression rate with Eq.3.28.

$$r = \phi r_{cl} \tag{3.28}$$

## 3.2 Paraffin-Mg-$CO_2$-$N_2O$ proposed configuration

Following the $CO_2$ combustion studies and the proposed metal powder-$CO_2$ rocket configuration, Karabeyoglu[24] noted that some issues related to it could be solved with a hydrocarbon binder and a mixture of $N_2O$ and $CO_2$ as oxidizer. The binder and the powder are mixed together forming a solid fuel grain, allowing for a classical hybrid rocket configuration and as a consequence removing the need of the complicated powder feeding system. The oxidizer mixture leads to the following advantages over the pure $CO_2$[24]:

- The specific impulse is improved (figure 3.4).
- The condensed mass fraction is reduced, reducing the two phase flow losses (figure 3.5).
- The hydrocarbon binder can be used. Burning with the $N_2O$ releases the metal particles that then burn with $CO_2$.
- Powder is more easily ignited and not only magnesium but even aluminum can be used increasing the specific impulse.
- $CO_2$ and $N_2O$ are miscible and have similar properties, with a low freezing temperature ideal for martian storage.

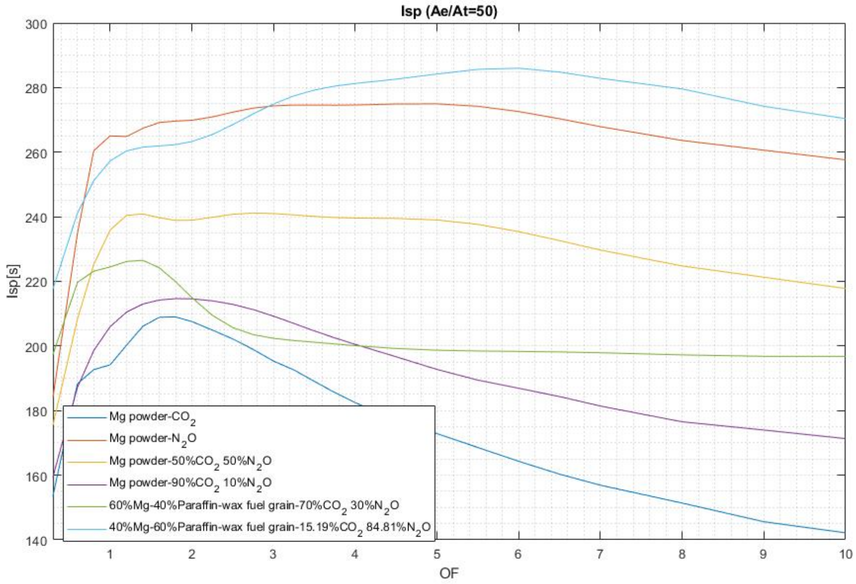

**Figure 3.4:** Specific Impulse for various Mg powder rockets /Mg+Paraffin hybrid rockets with different oxidizers and oxidizer mixtures[15][14]

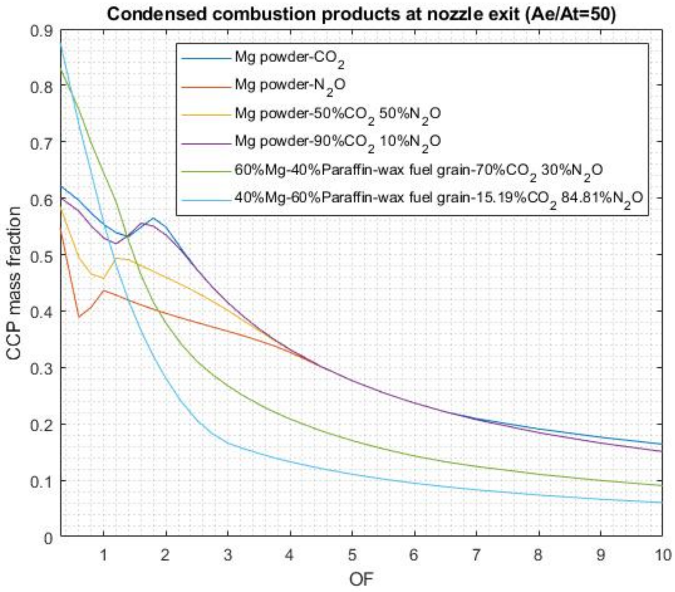

**Figure 3.5:** Condensed mass fraction at nozzle exit for various Mg powder rockets /Mg+Paraffin hybrid rockets with different oxidizers and oxidizer mixtures[15][14]

To have a higher volumetric efficiency (Eq.3.29) than classical hybrid propellants one, Karabenyoglu [24] proposed a paraffin binder. Thanks to the entrainment mechanism, paraffin based grains have a higher regression rate and can produce the desired flow rate (Eq.3.30), and as a consequence thrust (Eq.3.31), with less burning area, allowing for the use of grains with simpler geometry (i.e. single port grain design) and a more efficient fuel loading.

$$\eta_{V_g} = \frac{Volume\ of\ solid\ fuel}{Total\ volume\ of\ the\ grain} \tag{3.29}$$

$$\dot{m} = \dot{m}_o + \dot{m}_f = \dot{m}_o + rA_b\rho_f \tag{3.30}$$

$$F = \dot{m}c \tag{3.31}$$

### 3.2.1 Lab-scale motor tests

In [7], a saturated liquid $N_2O$-$CO_2$ mixture is proposed as oxidizer and tested with paraffin-$Mg$ and paraffin-$Al$ solid fuel grains. The paraffin fuel grains are cylindrical with a circular port and admixed with 44 $\mu m$ diameter $Mg$ powder up to 60% by mass. The tests are conducted with grains of two sizes, varying the percentage of $CO_2$ in the oxidizer mixture and the oxidizer flow rate. The oxidizer is injected in chamber head in blow down mode, maintaining an almost constant tank pressure thanks to oxidizer self pressurizing characteristics.

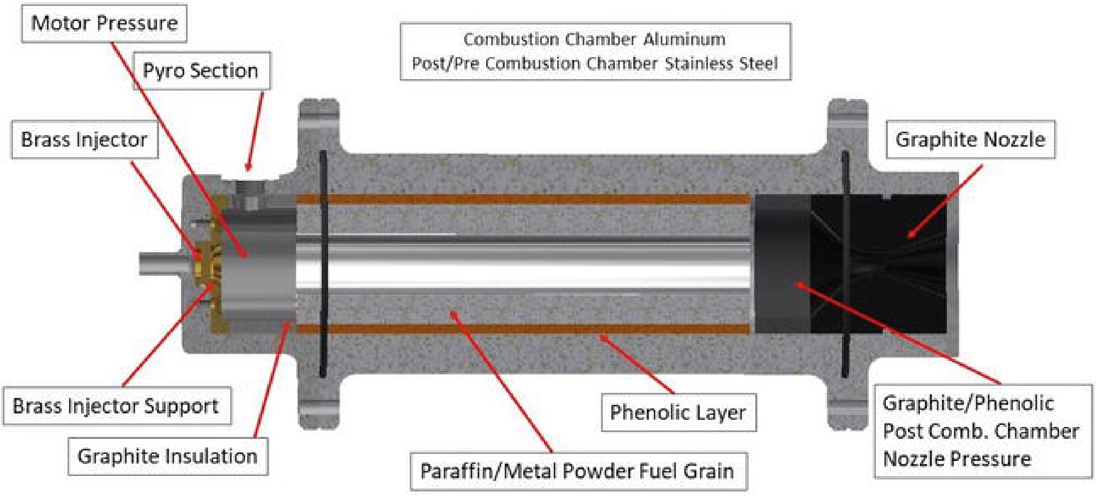

**Figure 3.6:** Kara's hybrid rocket motor layout[16]

### Ignition

The ignition is achieved by solid fuel pyro-igniter and an initial phase of pure $N_2O$ combustion needed to heat the chamber enough to allow $CO_2$ combustion to take place. With his experiments, Kara[25] was able to identify the ignition boundaries for the system in terms of oxidizer flux, $CO_2$ percentage and flame temperature. Increasing the percentage of $CO_2$ in the experiments oxidizer mixture, chamber temperature decreases as seen in figure 3.7[25] confirming CEA's[15][14] predictions in figure 3.8.

Figure 3.9 displays Kara's[25] experimental results finding no successful ignition for $CO_2$ percentages higher than 70/75% and a successful ignition zone in the oxidizer flux - $CO_2$ percentage space.

Figure 3.10 displays the theoretical ignition limit temperature for $Mg - CO_2$ around 1000 K found in previous researches, and a new temperature limit for $Mg$-paraffin $N_2O$-$CO_2$ system. Kara[16] explains this growth in temperature limit of 600 K or more, with the need for additional energy to vaporize the paraffin of the new system.

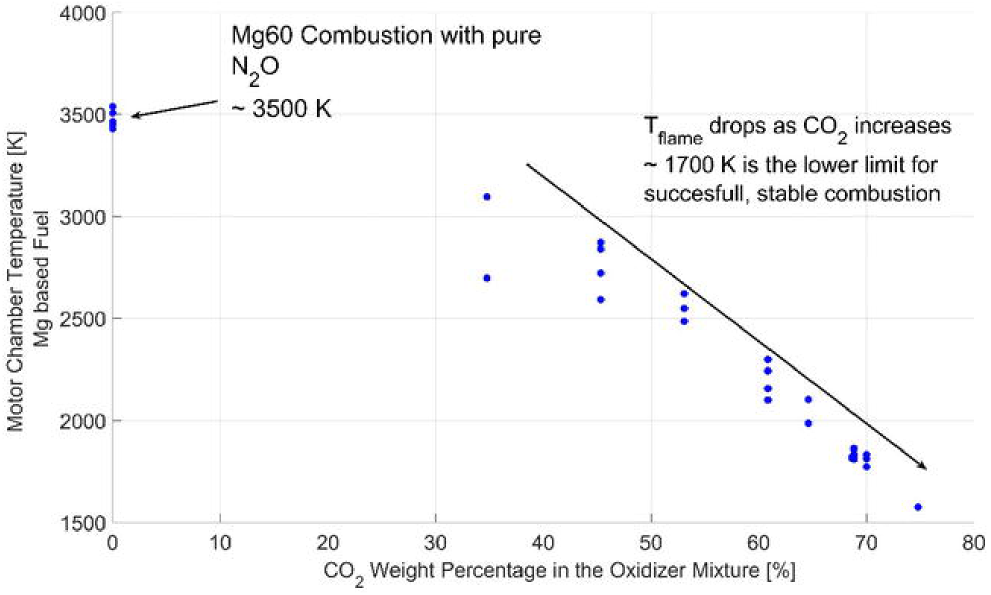

**Figure 3.7:** Chamber temperature variation with $CO_2$ percentage in the oxidizer mixture for paraffin-$Mg$ 60% fuel grain [25]

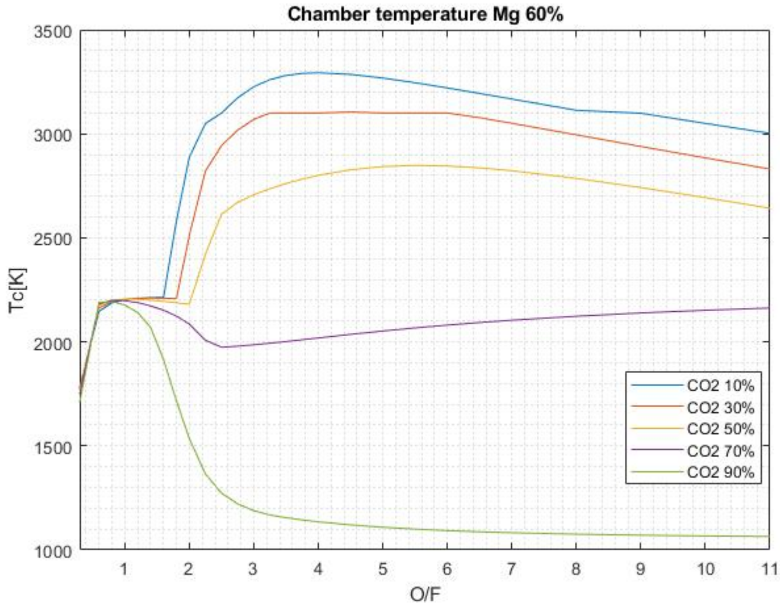

**Figure 3.8:** CEA predicted chamber temperature variation with $CO_2$ percentage in the oxidizer mixture and O/F for paraffin-$Mg$ 60% fuel grain

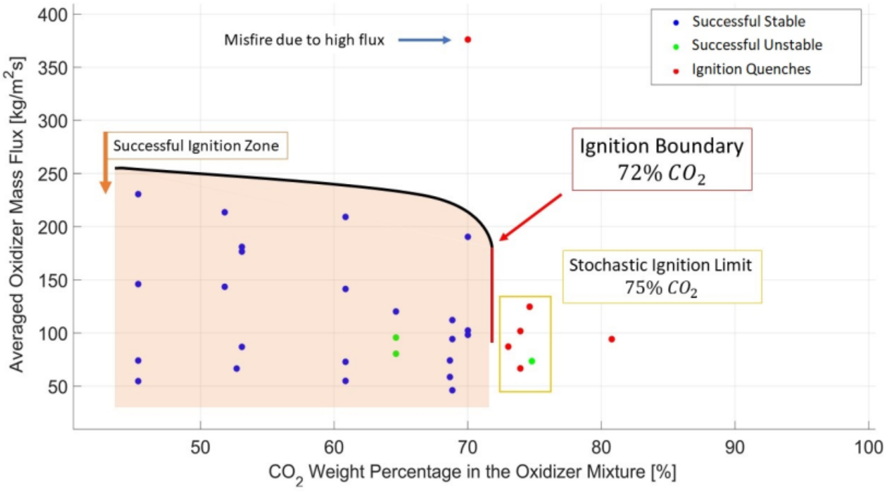

**Figure 3.9:** Ignition capability of experiments varying $CO_2$ fraction in the oxidizer mixture and oxidizer overall mass flux[25]

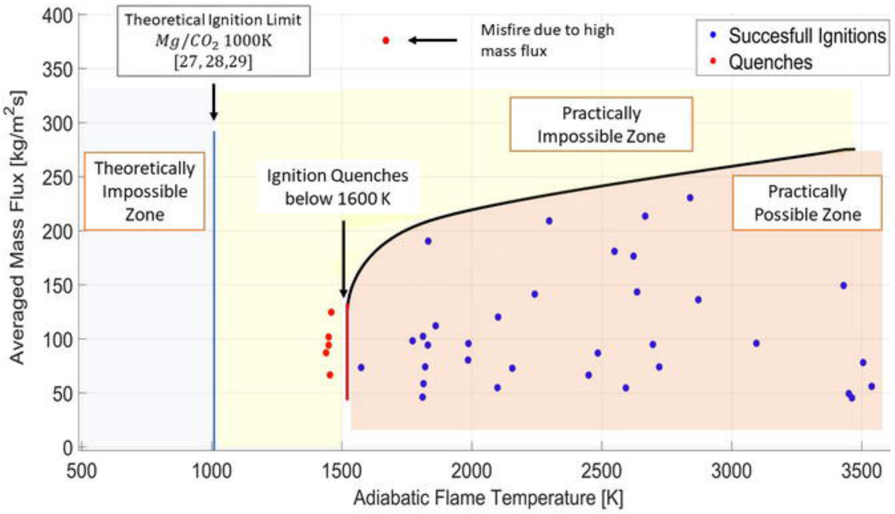

**Figure 3.10:** Ignition capability of experiments varying chamber temperature and mass flux[25]

### Magnesium oxide slag deposition

As seen in figure 3.5, the combustion of paraffin-$Mg$ and $N_2O$-$CO_2$ produces less, albeit not negligible, condensed combustion products with respect to the combustion of powder $Mg$ and $CO_2$. These particles deposit in the post-combustion chamber and nozzle throat[25] obstructing it and increasing chamber pressure. Kara[25] concluded that the oxide deposition has uniform-thin film characteristics noting, from the pressure time profiles of the experiments, that the mean injectors and chamber pressure difference was stable.

### Regression rate

The tests are conducted on small scale hybrid rocket motor, having a fuel grain length of 70 mm, outer diameter of 31 mm and port diameter of 13 mm, and scaled up hybrid rocket motor with a fuel grain length of 180 mm, outer diameter of 48 mm and port diameter of 24 mm. The small scale tests are named PCT (Propellant Characterization Tests), while the scaled up test are named MMT (Mars Motor Tests)[25]. The regression rate prediction is particularly complex, because the grain is made of liquefying heavily metal loaded fuel, with a fraction of the oxidizer not reacting with the binder but only with the additive. These propellant properties suggests the influence of pressure on the regression rate at low and high oxidizer fluxes (as in figure 3.11), due to the high metal content and consequent radiative heat contribution, and due to the $CO_2$ effect of slowing the chemical reactions between paraffin and $N_2O$ while reacting with metal particles.

The available regression rate data collected by Kara[25] can be seen in figure 3.12 and 3.13.

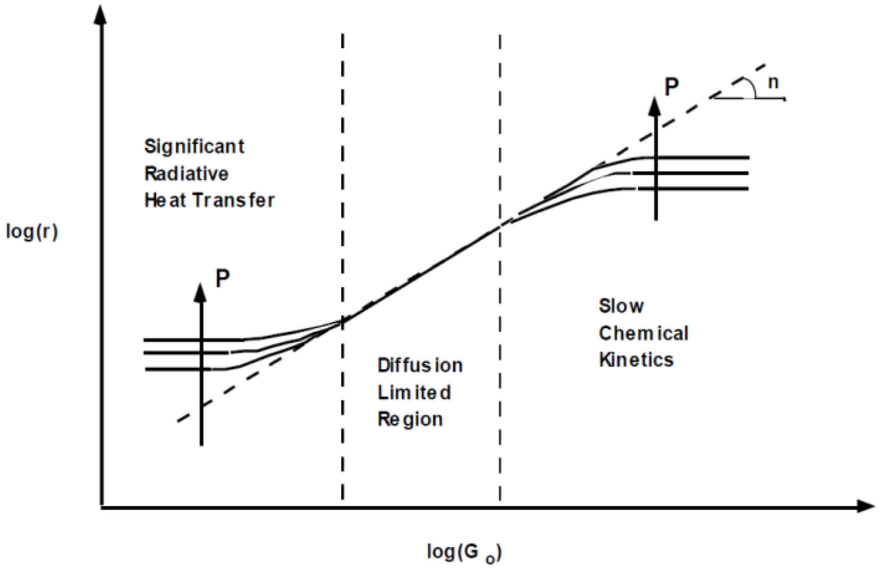

**Figure 3.11:** Effects of pressure on the regression rate [25]

In figure 3.14 the transformed regression rate data fit can be seen. The data are space averaged as suggested in [26], searching then the coefficients that better fit the transformed data to a regression rate law in the form of Eq.3.32, where r is in $\frac{mm}{s}$, $G_{ox}$ in $\frac{kg}{m^2 s}$ and L in $mm$. Using the given units of measure the coefficients are: $a = 30.3304$, $n = 0.1798$ and $m = -0.8786$ with a coefficient of determination $R^2 = 0.8611$.

$$r = aG_{ox}^{n}L^{m} \tag{3.32}$$

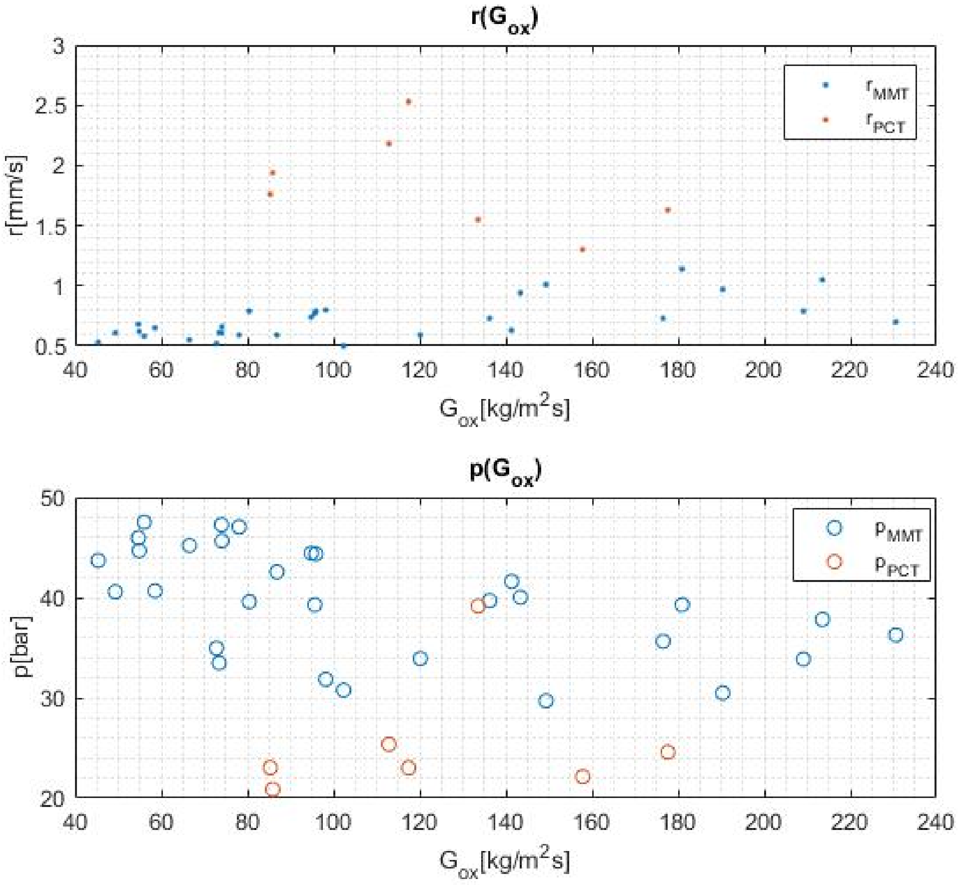

**Figure 3.12:** Mg-Paraffin grains regression rate and pressure experimental data [25]

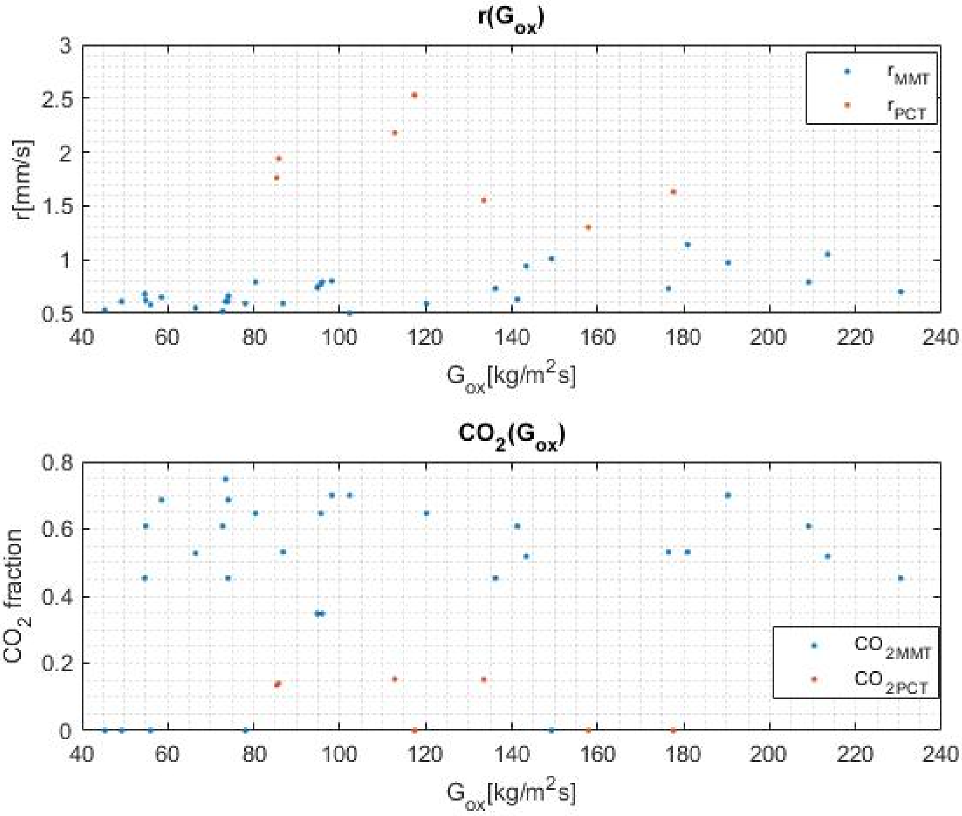

**Figure 3.13:** Mg-Paraffin grains regression rate and $CO_2$ mass fraction experimental data [25]

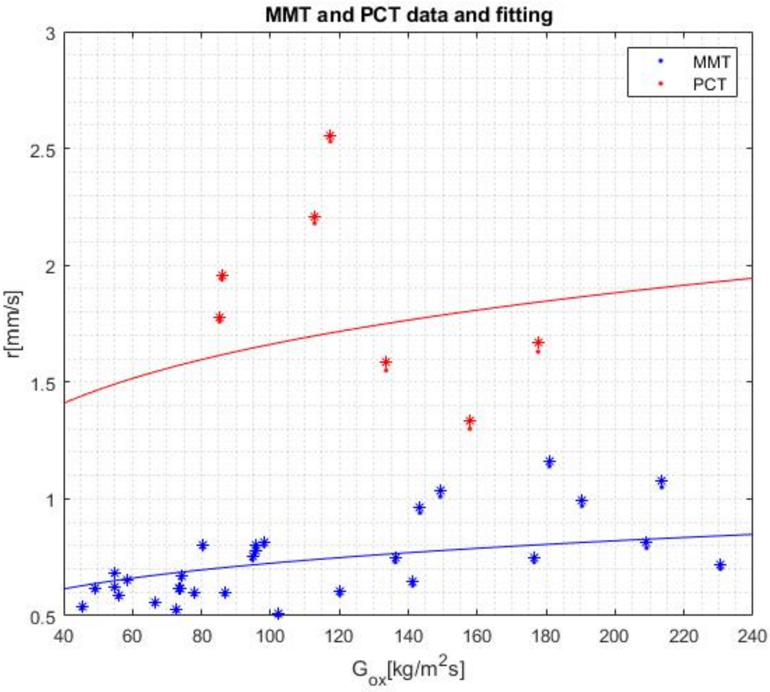

**Figure 3.14:** Mg-Paraffin data fit

# Chapter 4

# Mars Sample Return

The main application for which the $Mg$-$CO_2$ engine was designed is its use on Mars as propulsion system for a Mars Ascent Vehicle (MAV) or a Mars Hopper. As seen in Chapter 2, Mg-$CO_2$ combination is particularly advantageous for a Mars Hopper compared to classic storable propellants but, due to high condensed phase products and their deposition in the combustion chamber, a mission with a large number of ignitions such as that associated with a Mars Hopper may be difficult to complete without an adequate ignition reliability. A simpler application for the $Mg - CO_2$ engine can be as Mars Ascent Vehicle's propulsion system for a Mars Sample Return mission. A Mars Sample Return mission consist in sending a mission to the planet's surface, collecting samples and sending them back to Earth to be analyzed with more detail with respect to the capabilities of the instrumentation that can be sent to Mars. Mars Sample Return mission architectures can be divided in two families [27]:

- Direct return: the samples are placed into an Earth Return Vehicle (ERV) on the surface of Mars and routed toward Earth by it, not needing an additional vehicle in orbit.
- Rendezvous: the samples are placed into a Mars Ascent Vehicle that puts them in an orbit around Mars, where an Earth Return Vehicle collects them and performs the Mars-Earth transfer maneuver.

The Direct return architectures have the advantage of not involving an additional vehicle and the complexity of deep space rendezvous but the MAV needs to be much larger that in the Rendezvous case having to put into orbit not only the payload but also the propellant necessary to the low Mars orbit-Earth transfer. With a Rendezvous architecture a lighter MAV can be used, needing as a consequence to deliver less mass to Mars surface, but requiring and additional spacecraft capable to capture the samples' capsule or docking with it in orbit. The latter architecture is chosen, more easily achievable by the low specific impulse $Mg$-$CO_2$ engine.

## 4.1 $\Delta V$ requirements

To estimate the $\Delta V$ required to reach low Mars orbit, the ascent is simplified as an Hohmann transfer from the mean Mars radius to an orbit with an altitude of 400 km, ignoring the $\Delta V$ losses from gravity, aerodynamic and steering and the contribution to velocity from the rotation of the planet and increasing the $\Delta V$ found by 10%.

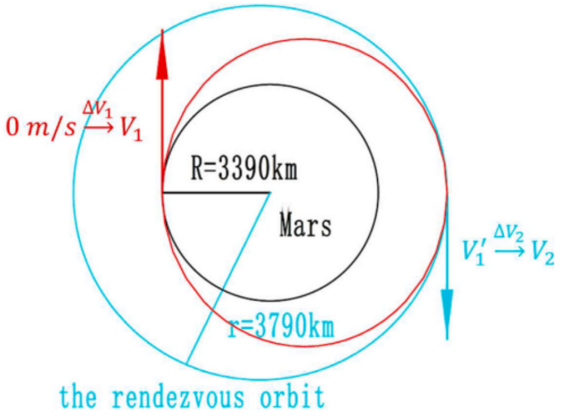

**Figure 4.1:** Hohmann transfer from martian surface to orbit with r=3790 km[28]

Mars has a mass of $M_{\mars} = 6.419\ 10^{23}\ kg$ and a mean radius of $R_{\mars} = 3390\ km$. Defined the standard gravitational parameter as the product of the gravitational constant $G = 6.67\ 10^{-11}\ \frac{Nm^2}{kg^2}$ and the mass of the planet $\mu_{\mars} = M_{\mars}G = 42815\ \frac{km^3}{s^2}$. Given the conservation of the total specific mechanical energy for a Keplerian Orbit in Eq.4.1, the velocities in the Hohmann transfer orbit can be written as function of the circular velocity at the considered radius Eq.4.2, of the semi-major axis, and of periapsis radius and apoapsis radius.

$$\frac{V^2}{2} - \frac{\mu}{r} = -\frac{\mu}{2a} \tag{4.1}$$

$$\frac{V_c^2}{2} - \frac{\mu}{r} = -\frac{\mu}{2r} \rightarrow V_c = \sqrt{\frac{\mu}{r}} \tag{4.2}$$

$$\frac{V_1^2}{2} - \frac{\mu_{\mars}}{R_{\mars}} = -\frac{\mu_{\mars}}{R_{\mars} + r_{dest}} \rightarrow V_1 = V_{cR_{\mars}}\sqrt{\frac{2r_{dest}}{R_{\mars} + r_{dest}}} = 3.651\ \frac{km}{s} \tag{4.3}$$

$$\frac{V_1^{\prime 2}}{2} - \frac{\mu_{\mars}}{r_{dest}} = -\frac{\mu_{\mars}}{R_{\mars} + r_{dest}} \rightarrow V_1^{'} = V_{cr_{dest}}\sqrt{\frac{2R_{\mars}}{R_{\mars} + r_{dest}}} = 3.266\ \frac{km}{s} \tag{4.4}$$

With the first burn at Mars surface, not taking into account the rotation of the planet, the spacecraft has to reach $V_1$ defined in Eq.4.3 starting from $V_0 = 0\ \frac{km}{s}$, so $\Delta V_1 = V_1 = 3.651\ \frac{km}{s}$. Reached the apoapsis of the transfer orbit at the desired target radius, a second burn is needed to circularize the orbit, to do so the spacecraft needs to reach the circular velocity at that radius starting from $V_1^{'}$, so $\Delta V_2 = V_{cr_{dest}} - V_1^{'} = 95\ \frac{m}{s}$. The total $\Delta V$ is assumed to be the sum of the two required for the burns increased by the 10% to account for the losses: $\Delta V = 1.1\left(\Delta V_1 + \Delta V_2\right) = 4.120\ \frac{km}{s}$.

This velocity change has to be delivered by the propulsion system that follows the Tsiolkovsky rocket equation 4.5, where $c = I_{sp} g_0$ is the effective exhaust velocity ($I_{sp}$ is the specific impulse and $g_0$ is the standard gravity acceleration at Earth sea level), $m_0$ and $m_{fin}$ respectively are the masses of the spacecraft before and after providing the $\Delta V$.

$$\Delta V = c \ln\left(\frac{m_0}{m_{fin}}\right) = I_{sp} g_0 \ln\left(\frac{m_0}{m_{fin}}\right) = -I_{sp} g_0 \ln\left(\frac{m_{fin}}{m_0}\right) \tag{4.5}$$

$$m_0 = m_{pay} + m_p + m_s = m_{fin} + m_p; \qquad m_{fin} = m_{pay} + m_s; \tag{4.6}$$

Where $m_{pay}$ is the payload mass, $m_s$ is the structural mass and $m_p$ is the propellant mass. It's convenient to define two parameters to rewrite the mass fraction in Eq.4.5: a payload fraction $\lambda$ and a structural parameter $\epsilon$.

$$\lambda = \frac{m_{pay}}{m_0} \tag{4.7}$$

$$\epsilon = \frac{m_s}{m_s + m_p} \tag{4.8}$$

Using these parameters Eq.4.5 can be written as:

$$\Delta V = -c \ln\left(\lambda\left(1 - \epsilon\right) + \epsilon\right) \tag{4.9}$$

From Eq.4.9 is possible to explicit $\lambda$ as a function of $\epsilon$ and $\frac{\Delta V}{c}$:

$$\lambda = \frac{e^{-\frac{\Delta V}{c}} - \epsilon}{1 - \epsilon} \tag{4.10}$$

To have a payload, $\lambda$ has to be grater than zero so, being $\epsilon < 1$:

$$e^{-\frac{\Delta V}{c}} - \epsilon > 0 \rightarrow \epsilon < e^{-\frac{\Delta V}{c}} \tag{4.11}$$

For a given mission ($\Delta V$) and propellant ($c$), Eq.4.11 determines the limit value for the structural coefficient to make the mission possible. If it's impossible to reach the structural coefficient's needed value, the mission $\Delta V$ has to be split between multiple sub-rockets with staging. For a N-stage rocket Eq.4.9 can be written as:

$$\Delta V = \sum_{j=1}^{N} \Delta V_j = \sum_{j=1}^{N} -c_j \ln \left( \frac{m_{finj}}{m_{0j}} \right) = \sum_{j=1}^{N} -c_j \ln \left( \lambda_j \left( 1 - \epsilon_j \right) + \epsilon_j \right) \tag{4.12}$$

For each sub-rocket the parameters definitions are the same of above with the payload mass of a sub-rocket being the initial mass of the next one. The total payload fraction can then be written as:

$$\lambda_{tot} = \frac{m_{pay}}{m_0} = \frac{m_{pay}}{m_{0N}} \frac{m_{0N}}{m_{0(N-1)}} \cdots \frac{m_{03}}{m_{02}} \frac{m_{02}}{m_0} = \prod_{j=1}^{N} \lambda_j \tag{4.13}$$

With $\lambda_j$ in the same form of $\lambda$:

$$\lambda_j = \frac{e^{-\frac{\Delta V_j}{c_j}} - \epsilon_j}{1 - \epsilon_j} \tag{4.14}$$

## 4.2 Fraction between payload mass and mass sent from Earth

Due to the nature of Mars Sample Return mission, there is the interest of maximizing the ratio between the payload mass of the MAV and the mass of it sent from Earth to make the mission more cost effective. The mass fraction can be written as in Eq. 4.15 using $\lambda_{tot}$.

$$\frac{m_{pay}}{m_E} = \frac{m_{pay}}{m_0} \frac{m_0}{m_E} = \lambda_{tot} \frac{m_0}{m_E} \tag{4.15}$$

Where $m_{pay}$ is the payload mass of the MAV, $m_0$ is the initial mass of the MAV prior to its ascent to martian orbit and $m_E$ is the mass of the MAV sent from Earth defined as follows:

$$m_E = m_s + \chi_{ox} m_{ox} + \chi_f m_f = m_d - m_{pay} + \chi_{ox} m_{ox} + \chi_f m_f \tag{4.16}$$

Where $m_{ox}$ and $m_f$ are MAV's oxidizer and fuel masses prior to its ascent to martian orbit, $\chi_{ox} = \frac{m_{oxE}}{m_{ox}}$ and $\chi_f = \frac{m_{fE}}{m_f}$ are the mass fractions of oxidizer and fuel sent from Earth, $m_s$ is the structural mass of the MAV and $m_d$ is its dry mass defined in Eq.4.17.

$$m_d = m_0 - m_p = m_s + m_{pay} \tag{4.17}$$

$$OF = \frac{m_{ox}}{m_f} \tag{4.18}$$

Defined the oxidizer to fuel ratio OF in Eq.4.18 is possible to write the oxidizer mass and the fuel mass as a function of the propellant mass ($m_p$) (Eq.4.19).

$$m_f = \frac{1}{(1+OF)} m_p \quad \& \quad m_{ox} = \frac{OF}{(1+OF)} m_p \tag{4.19}$$

Using Eq.4.17 and Eq.4.19 is possible to write $m_E$ as:

$$m_E = m_0 - m_{pay} + \left( \frac{\chi_{ox} OF + \chi_f}{1+OF} - 1 \right) m_p \tag{4.20}$$

Dividing it by $m_0$:

$$\frac{m_E}{m_0} = 1 - \lambda_{tot} + \left( \frac{\chi_{ox} OF + \chi_f}{1+OF} - 1 \right) \frac{m_p}{m_0} \tag{4.21}$$

Using the rocket equation the propellant mass for each stage can be written as:

$$m_{pj} = m_{0j} - m_{finj} = \left( 1 - e^{-\frac{\Delta V_j}{c_j}} \right) m_{0j} \tag{4.22}$$

And the total propellant mass:

$$m_p = \sum_{j=1}^{N} m_{pj} = \sum_{j=1}^{N} \left( 1 - e^{-\frac{\Delta V_j}{c_j}} \right) m_{0j} \tag{4.23}$$

Substituting in Eq.4.21:

$$\frac{m_E}{m_0} = 1 - \lambda_{tot} + \left( \frac{\chi_{ox} OF + \chi_f}{1+OF} - 1 \right) \frac{1}{m_0} \sum_{j=1}^{N} \left( 1 - e^{-\frac{\Delta V_j}{c_j}} \right) m_{0j} \tag{4.24}$$

Noting that $m_0 = m_{01}$ and that for $j > 1$:

$$m_{0j} = m_0 \prod_{i=1}^{j-1} \lambda_i \tag{4.25}$$

Eq. 4.24 can be rewritten as:

$$\frac{m_E}{m_0} = 1 - \lambda_{tot} + \left( \frac{\chi_{ox} OF + \chi_f}{1+OF} - 1 \right) \left( 1 - e^{-\frac{\Delta V_1}{c_1}} + \sum_{j=2}^{N} \left( 1 - e^{-\frac{\Delta V_j}{c_j}} \right) \prod_{i=1}^{j-1} \lambda_i \right) \tag{4.26}$$

And finally substituting in Eq.4.15:

$$\frac{m_{pay}}{m_E} = \frac{\lambda_{tot}}{1 - \lambda_{tot} + \left( \frac{\chi_{ox} OF + \chi_f}{1+OF} - 1 \right) \left( 1 - e^{-\frac{\Delta V_1}{c_1}} + \sum_{j=2}^{N} \left( 1 - e^{-\frac{\Delta V_j}{c_j}} \right) \prod_{i=1}^{j-1} \lambda_i \right)} \tag{4.27}$$

The mass fraction in Eq. 4.27 depends on the number of stages $N$, on the stages' properties as $\Delta V$ allocation and on propellant combination's properties as $OF$, $c(OF)$ and mass fractions of oxidizer $\chi_{ox}$ and fuel $\chi_f$ brought from Earth. In $\lambda$ there is also the dependence on the structural parameter. Given the stages and propellant combination's properties it's possible to search the $OF$ that maximizes the payload mass fraction.

### 4.2.1 Stages with same properties

If each stage has the same properties $c_j$,$\epsilon_j$,$\Delta V_j$, $\lambda_j$ is also the same. In this case Eq.4.13 becomes:

$$\lambda_{tot} = \prod_{j=1}^{N} \lambda_j = \prod_{j=1}^{N} \lambda = \lambda^N \tag{4.28}$$

Noting that for $\lambda_j = \lambda$:

$$\sum_{j=1}^{N} m_{0j} = m_0 + \lambda m_0 + \lambda^2 m_0 \cdots \lambda^{N-1} m0 = m_0 \sum_{j=1}^{N} \lambda^{j-1} \tag{4.29}$$

and that $\Delta V_j = \frac{\Delta V}{N}$ Eq.4.23 becomes:

$$m_p = \sum_{j=1}^{N} \left(1 - e^{-\frac{\Delta V_j}{c_j}}\right) m_{0j} = \left(1 - e^{-\frac{\Delta V}{Nc}}\right) m_0 \sum_{j=1}^{N} \lambda^{j-1} \tag{4.30}$$

And as a consequence Eq. 4.15:

$$\frac{m_{pay}}{m_E} = \frac{\lambda^N}{1 - \lambda^N + \left(\frac{\chi_{ox} OF + \chi_f}{1+OF} - 1\right)\left(1 - e^{-\frac{\Delta V}{Nc}}\right) \sum_{j=1}^{N} \lambda^{j-1}} \tag{4.31}$$

## 4.3 Estimating the structural parameter

To compare various propellants and designs it is useful to estimate the structural parameter $\epsilon$. To do this, noting that the mass of the pressurized tanks can be written as a function of the properties of the propellants and oxidizer to fuel ratio, it is useful to assume that the structural mass is approximately equal to that of the tanks. The structural parameter becomes:

$$\epsilon = \frac{m_s}{m_s + m_p} \approx \frac{m_t}{m_t + m_p} \tag{4.32}$$

The tanks mass can be expressed as a function of the propellant volume contained:

$$m_t = K_t \frac{m_p}{\rho_p} \tag{4.33}$$

Where $K_t$ is defined as the ratio between the mass of the tanks and the volume of propellant contained and $\rho_p$ is the bulk density.

$$\rho_p = \frac{(1 + OF)\,\rho_f \rho_{ox}}{\rho_{ox} + OF\rho_f} \tag{4.34}$$

Substituting 4.33 in 4.32:

$$\epsilon = \frac{K_t \frac{m_p}{\rho_p}}{K_t \frac{m_p}{\rho_p} + m_p} = \frac{\frac{K_t}{\rho_p}}{\frac{K_t}{\rho_p} + 1} \tag{4.35}$$

For each stage $K_t$ can be written as:

$$K_t = \frac{m_{tf} + m_{tox}}{V_f + V_{ox}} = \frac{k_{tf} + k_{tox} OF \frac{\rho_f}{\rho_{ox}}}{1 + OF \frac{\rho_f}{\rho_{ox}}} \tag{4.36}$$

Where $k_{tf}$ and $k_{tox}$ have the same definition as $K_t$ but for the single tanks. $k_t$ can be estimated knowing the tank geometry, material and pressure of work as suggested by Humble[17].

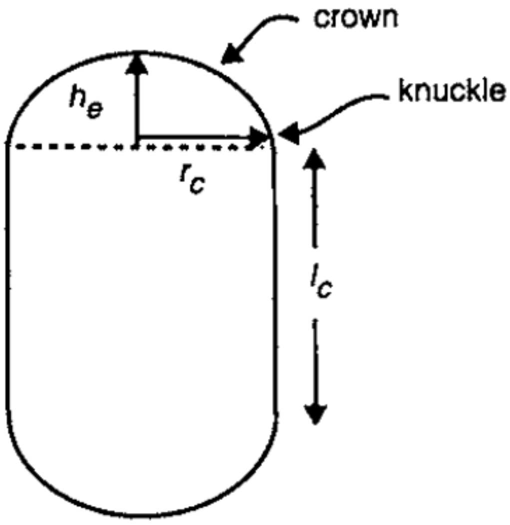

**Figure 4.2:** Geometry of the cylindrical tank [17]

Assuming spherical or cylindrical with spherical ends tanks (figure 4.2 with $h_e = r_c$), $k_t$ is calculated as follows:

- Thickness estimate from equilibrium at burst pressure $p_b$ (defined as the maximum working pressure of the tank increased by a safety factor), describing the geometry of the tank with a radius and an elongation $el = \frac{l_c}{r_c}$

$$(2\pi r_c t + 2l_c t)\,\sigma_{mat} = \left(\pi r_c^2 + 2l_c r_c\right) p_b \rightarrow t = \frac{(\pi + 2el)\, r_c}{2\,(\pi + el)} \frac{p_b}{\sigma_{mat}} \tag{4.37}$$

With $\sigma_{mat}$ is the maximum allowable material strength.

- Calculating mass and volume of the tank:

$$m_t = A_t t \rho_{mat} = 2\pi r_c^2\,(2 + el)\, t \rho_{mat} = \frac{\pi r_c^3\,(\pi + 2el)\,(2 + el)}{(\pi + el)} \frac{\rho_{mat} p_b}{\sigma_{mat}} \tag{4.38}$$

$$V_t = \pi r_c^3 \left(\frac{4}{3} + el\right) \tag{4.39}$$

- Estimating $k_t$ using its definition and a volumetric loading efficiency $\eta_v = \frac{V_p}{V_t}$:

$$k_t = \frac{m_t}{V_p} = \frac{m_t}{\eta_v V_t} = \frac{(\pi + 2el)\,(2 + el)}{\eta_v \left(\frac{4}{3} + el\right)(\pi + el)} \frac{\rho_{mat} p_b}{\sigma_{mat}} \tag{4.40}$$

From Eq.4.35, 4.36 and 4.40 can be seen that, chosen the geometry, material, pressure of work and volumetric loading efficiency of the tanks, $\epsilon$ is only a function of OF and density ratio of propellants. Chosen the propellants, $\epsilon$ is a function only of OF and as a consequence for a multistage rocket with stages with same properties, being $c = c(OF)$ and chosen the mission, $\lambda_j = \lambda$ is only a function of the OF and number of stages N.

$$\lambda(OF) = \frac{e^{-\frac{\Delta V}{Nc(OF)}} - \epsilon(OF)}{1 - \epsilon(OF)} \tag{4.41}$$

As a consequence $\frac{m_{pay}}{m_E}$ for a mission, it's a function only of the OF, number of stages and fractions of propellants brought from the Earth.

# Chapter 5

# Comparison of propellants and ISRU options for a Mars Ascent Vehicle

In this chapter are compared the performances of the Powder Mg-$CO_2$ rocket, of the Paraffin-Mg-$CO_2$-$N_2O$ rocket and of some others Mg-storable oxidizer combinations maximizing the fraction $\frac{m_{pay}}{m_E}$ for a Mars Ascent Vehicle, for various ISRU options. Engine performances like the specific impulse are calculated with CEA[15][14] shifting equilibrium analysis, with a nozzle expansion ratio $\varepsilon_n$ of 50 and a chamber pressure $p_c$ of 1 MPa.

## 5.1 Engine mass fraction

Being the Powder rocket engine configuration similar to that of a liquid rocket engine while the Paraffin-Mg rocket has a classical hybrid configuration, an engine mass fraction $k_e = \frac{m_{engine}}{m_0}$ is used to take into account their differences. Doing so, the structural parameter becomes:

$$\epsilon_j = \frac{K_t \frac{m_{pj}}{\rho_p} + k_e m_{0j}}{K_t \frac{m_{pj}}{\rho_p} + k_e m_{0j} + m_{pj}} = \frac{\left(\frac{K_t}{\rho_p}\right)_{eq}}{\left(\frac{K_t}{\rho_p}\right)_{eq} + 1} \tag{5.1}$$

Where:

$$\left(\frac{K_t}{\rho_p}\right)_{eq} = \frac{K_t}{\rho_p} + \frac{k_e}{1 - e^{-\left(\frac{\Delta V}{Nc}\right)}} \tag{5.2}$$

$k_e$ is estimated for the powder engine, starting from the liquid launch-vehicle engines relation given by Humble[17] as:

$$k_e = \frac{g_{♂} TWR_{♂}}{g_0 \left(0.0006098 m_0 g_{♂} TWR_{♂} + 13.44\right)} \tag{5.3}$$

Where $g_{♂}$ and $g_0$ are the gravity accelerations at Mars and Earth surface, $TWR_{♂}$ is the thrust to weight ratio of the rocket stage on Mars and $m_0$ is the initial mass of the stage. To simplify the estimate a constant value of $k_e$ is chosen assuming a $TWR_{♂}$ for the stage and an initial stage mass. The initial mass, supposing to design a Mars ascent vehicle for a Mars sample return mission, can be expected to be around 500 kg as that proposed in [29], with a $TWR_{♂}$ grater than 1. From figure 5.1, a conservative value could be $k_e = 0.05$.

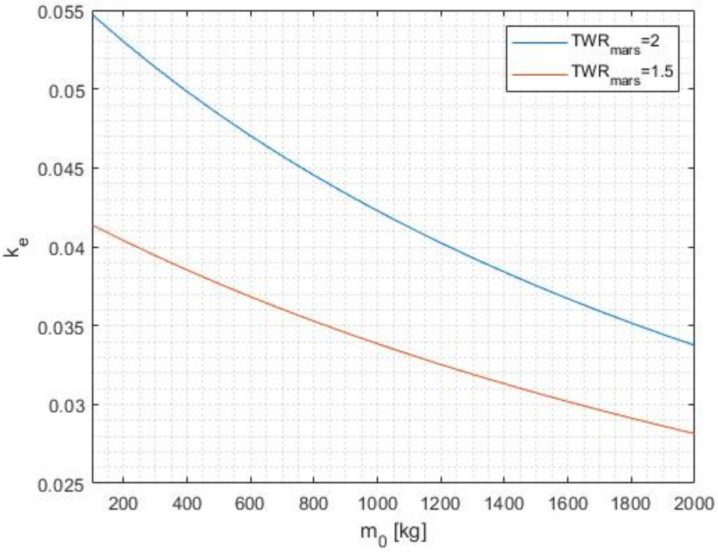

**Figure 5.1:** Liquid Engine mass fraction

For the hybrid rocket, the combustion chamber is also the fuel tank and therefore its mass has already been counted. To take account of the nozzle $k_e$ is estimated starting by the hybrid rocket nozzle relation given by Humble[17] as:

$$k_e = \frac{125}{m_0^{\frac{1}{3}}} \left(1 - e^{-\left(\frac{\Delta V}{Nc}\right)}\right)^{\frac{2}{3}} \left(\frac{\varepsilon_n}{10}\right)^{\frac{1}{4}} \tag{5.4}$$

Where $\varepsilon_n = \frac{A_e}{A_t}$ is the nozzle expansion ratio. In this context, it is convenient to take a constant $k_e$ value, like for the powder rocket. Assumed an initial mass of 500 kg and nozzle expansion ratio of 50, from figure 5.2 a conservative value could be $k_e = 0.065$.

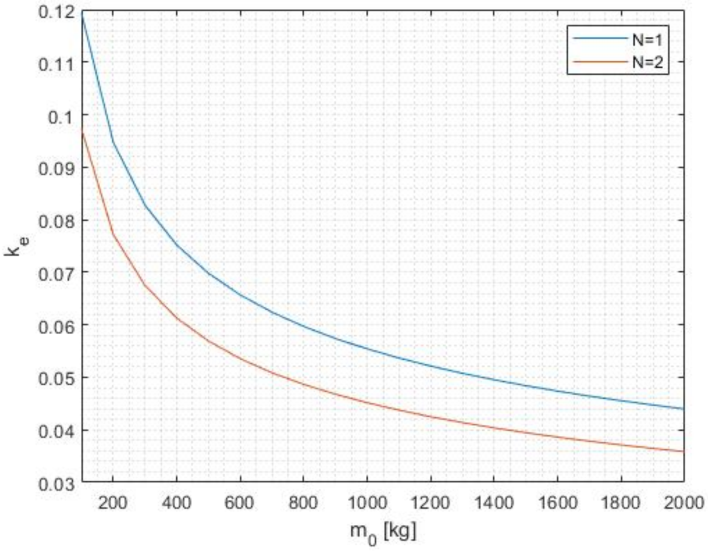

**Figure 5.2:** Hybrid rocket nozzle mass fraction for $\varepsilon_n = 50$

## 5.2 ISRU options

The study focuses on the $Mg - CO_2$ combination given the easy availability of $CO_2$ on Mars, the relative ease of ignition of Mg in it and the future possibility of producing magnesium from martian regolith. For the advantages seen in Chapter 3, the viability of a paraffin based magnesium hybrid rocket is analyzed. In addition $Mg - N_2O$, $Mg - N_2O_4$ and $Mg - CO_2 - N_2O$ combinations are considered. The ISRU options considered are:

- Capture of $CO_2$ from martian atmosphere ($CO_2 \approx 97\%, N_2 \approx 3\%$);

- Capture of $CO_2$ and/or production of magnesium powder on Mars;

Moreover the case without ISRU is analyzed as reference. For the propellants combinations considered, the options can be summarized in Table 5.1:

| Propellants | $CO_2$ capture | $CO_2$ capture and/or $Mg$ production | Without ISRU |
|---|---|---|---|
| $Mg$-$CO_2$ | ● $CO_2$ | ● $CO_2$ & $Mg$ | ● |
| $Mg$-$N_2O$ |  | ● $Mg$ | ● |
| $Mg$-$N_2O_4$ |  | ● $Mg$ | ● |
| $Mg$-$CO_2$-$N_2O$ | ● $CO_2$ | ● $CO_2$ & $Mg$ | ● |
| $Mg$-Paraffin-$CO_2$-$N_2O$ | ● $CO_2$ | ● $CO_2$ & $Mg$ | ● |

**Table 5.1:** Analyzed options

## 5.3 Comparison

Due to the high condensed combustion products mass fraction, the performances are evaluated at the two extremes:

- Best case: the exchange of heat and momentum between gas and particles is good and the two-phase flow losses are negligible.

- Worst case: there is no heat and momentum exchange between gas and particles and the latter do not contribute to the thrust.

For the best case the ideal effective exhaust velocities calculated by CEA are used, while for the worst case these latter are reduced multiplying them to the gaseous mass fraction as in Eq. 5.5, where $c_{id}$ is the velocity predicted by CEA and $\chi_{CCP}$ is the Condensed Combustion Products mass fraction at the nozzle exit.

$$c = c_{id}\,(1 - \chi_{CCP}) \tag{5.5}$$

For the comparison the following is assumed:

- The stages have same propellant composition, same properties and $\Delta V$;

- Circular equatorial martian target orbit with 500 km altitude;

- Chamber pressure of 1 $MPa$ to limit nozzle non-adaptation with a limited nozzle expansion ratio, the martian low atmospheric pressure ranging between 6.9 and 10 mbar [2];

- Maximum oxidizer tank pressure of 10 $MPa$ to feed the oxidizer in blowdown and maintain it in a liquid state for a wide range of temperatures (figure 5.4);

- Maximum fuel tank pressure of 2 $MPa$ for the powder rocket, to have enough pressure difference to transport the fluidized powder into the chamber;
- Carbon fiber tanks: $\rho_{mat} = 1550\ \frac{kg}{m^3}$, $\sigma_{mat} = 850\ MPa$[17];
- Security factor=1.2 to increase maximum pressures[17];
- Estimated tanks masses doubled as suggested by Hubble[17];
- Density of magnesium powder= 0.74 of that of magnesium, assuming near maximum packing of equal spheres;
- Volumetric loading efficiencies $\eta_v$ of the powder tank and of the grain fuel equal to 0.8. Part of the volume of the powder tank is occupied by the actuation chamber decreasing $\eta_v$ from 1 to 0.8, while for the hybrid combustion chamber an optimistic $\eta_v$ value is chosen due to the paraffin based grain composition and a possible single port grain design;
- Elongation $el = 10$, being $k_t(el = 10)$ almost 90% of its asymptotic value (figure 5.3). Choosing this elongation value, a higher mass is estimated for the tanks, leaving a greater margin for the structural mass for the subsequent design phases;
- Mixtures of fuels or oxidizers with constant volume → $\rho_{mix} = \frac{\rho_1 \rho_2}{\rho_1 + \chi_1(\rho_2 - \rho_1)}$. Where $\chi_1 = \frac{m_1}{m_{mix}}$ is the mass fraction of mixture's component 1.

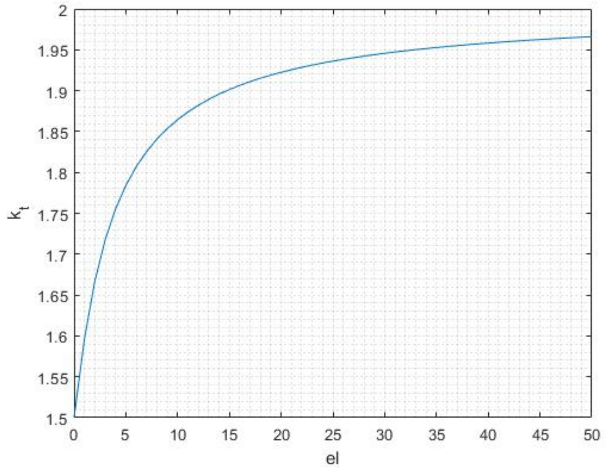

**Figure 5.3:** $k_t$ for $\eta_v = 1$, $\rho_{mat} = 1$ and $\sigma_{mat} = p_b$

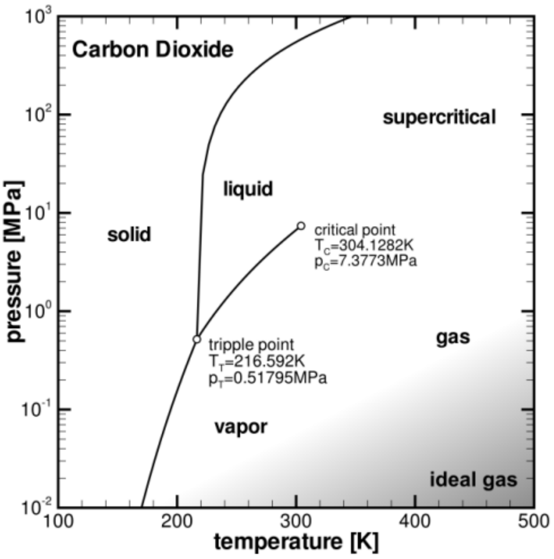

**Figure 5.4:** $CO_2$ phase diagram[30]

For the $Mg$-$CO_2$-$N_2O$ case and for the Paraffin-$Mg$-$CO_2$-$N_2O$ case, the optimal composition of the grain and/or of the oxidizer mixture is found comparing different mixtures for each case without taking account of the engine weight, using the same engine type for every composition.

### 5.3.1 $Mg$-$CO_2$-$N_2O$

Using the Powder $Mg$ rocket configuration with a mixture of $CO_2$ and $N_2O$ as oxidizer, all the three ISRU options are theoretically available. The results are shown below as maximum $\frac{m_{pay}}{m_E}$, function of the $N_2O$'s percentage in the mixture, for the case with and without two phase flow losses.

#### $Mg$-$CO_2$-$N_2O$ without losses

Figure 5.5 shows the effective exhaust velocity trend varying the $CO_2$ concentration in the mixture. For a mission without ISRU is clear that the best option is using only $N_2O$ as oxidizer, as can be seen in figure 5.6, with an increase around 2% of the payload with a two-stage rocket over the single stage one. If it's possible to collect the $CO_2$ on Mars, the best option is to use only $CO_2$ as oxidizer (figure 5.7). The same is true if it's possible to produce even the $Mg$ powder (figure 5.8).

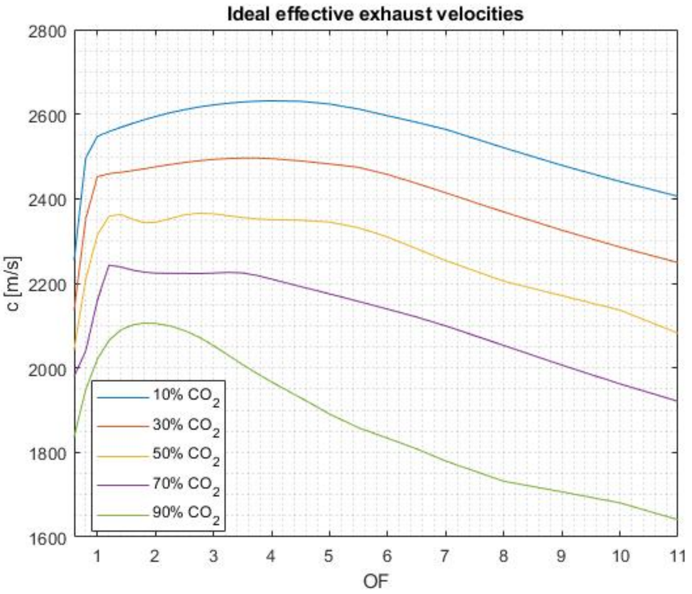

**Figure 5.5:** Ideal effective exhaust velocity varying the $CO_2$ mass fraction in the oxidizer mixture

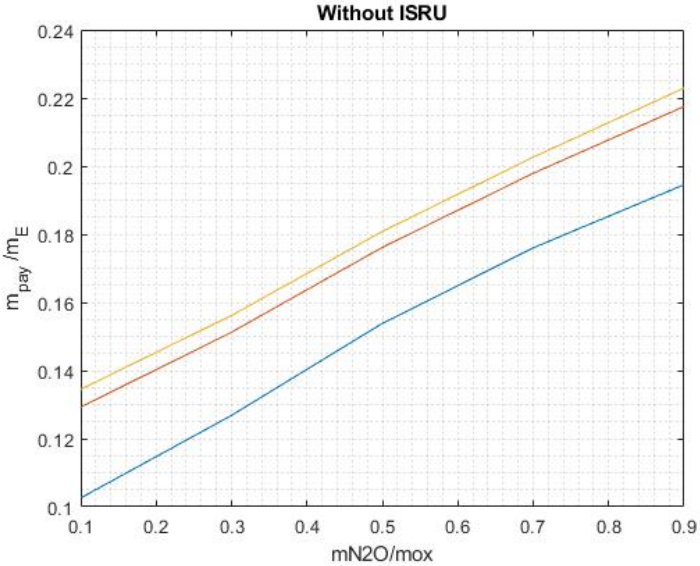

**Figure 5.6:** Maximum $\frac{m_{pay}}{m_E}$ without ISRU varying $N_2O$ % in the oxidizer mixture for a single stage (blue), a two stage (red) and a three stage (yellow) rocket

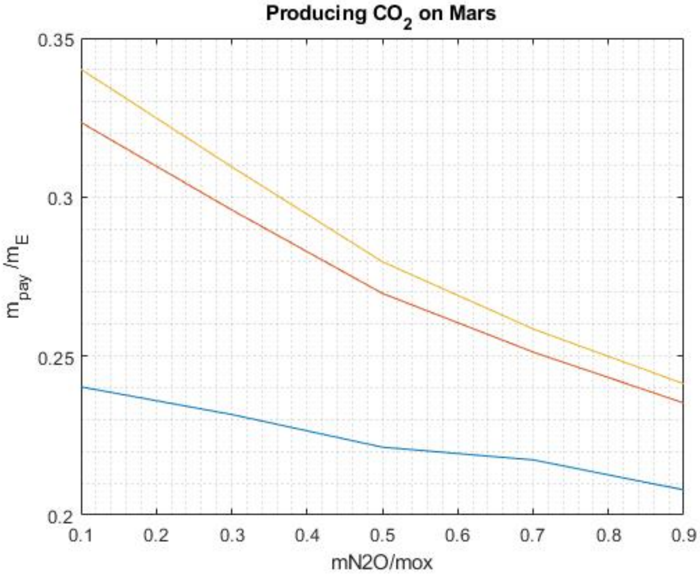

**Figure 5.7:** Maximum $\frac{m_{pay}}{m_E}$ collecting the $CO_2$ on Mars, varying $N_2O$ % in the oxidizer mixture for a single stage (blue), a two stage (red) and a three stage (yellow) rocket

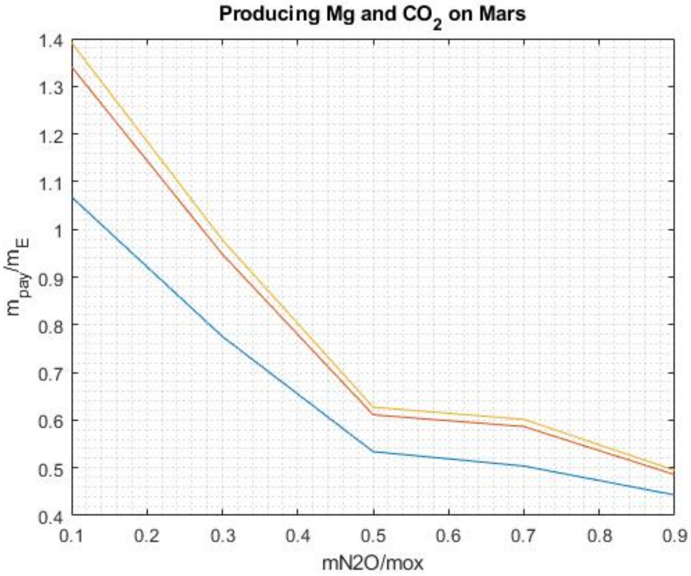

**Figure 5.8:** Maximum $\frac{m_{pay}}{m_E}$ collecting the $CO_2$ and $Mg$ on Mars, varying $N_2O$ % in the oxidizer mixture for a single stage (blue), a two stage (red) and a three stage (yellow) rocket

### $Mg$-$CO_2$-$N_2O$ with losses

Even at its minimum, Condensed Combustion Products mass fraction at nozzle exit it's not negligible (figure 5.9). The maximum effect that the two-phase flow can have on the effective exhaust velocity is to reduce it by the CCP mass fraction (eq. 5.5), leading to the effective exhaust velocities in figure 5.10.

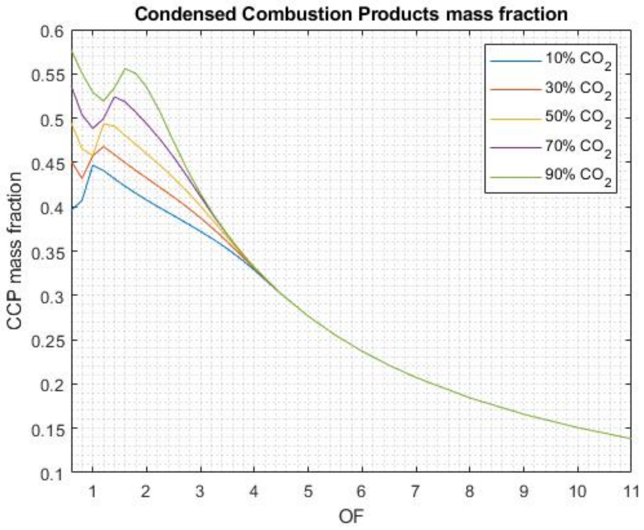

**Figure 5.9:** CCP mass fraction at nozzle exit varying $CO_2$ percentage in the oxidizer mixture and OF

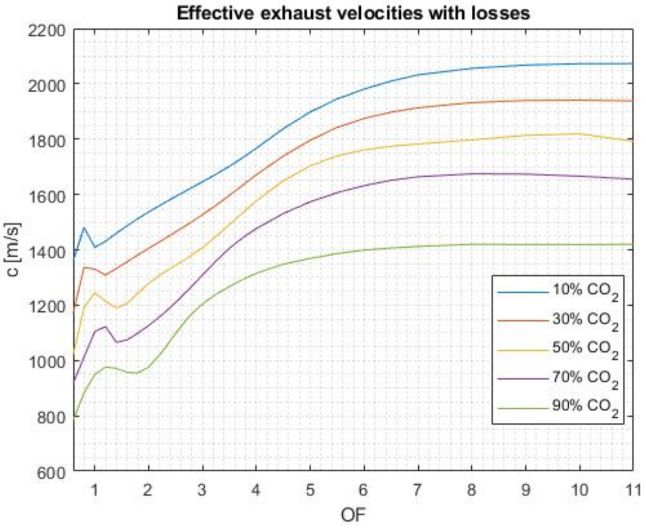

**Figure 5.10:** Effective exhaust velocities with maximum two-phase flow losses

As for the ideal case, for a mission without ISRU the best option is to use only $N_2O$ as oxidizer (figure 5.11).

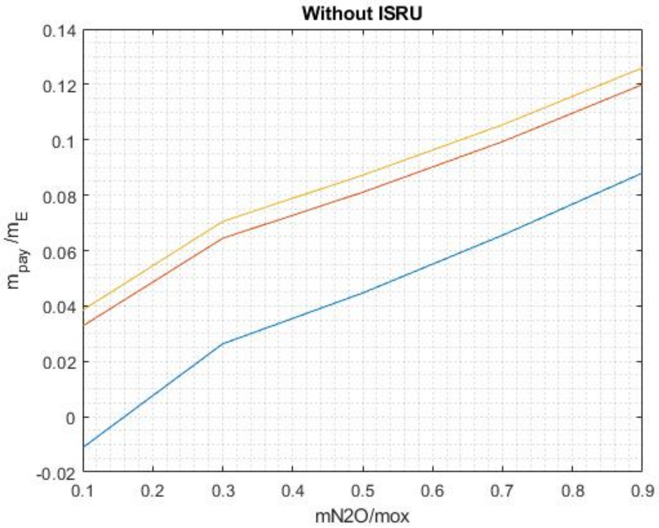

**Figure 5.11:** Maximum $\frac{m_{pay}}{m_E}$ with losses without ISRU varying $N_2O$ % in the oxidizer mixture for a single stage (blue), a two stage (red) and a three stage (yellow) rocket

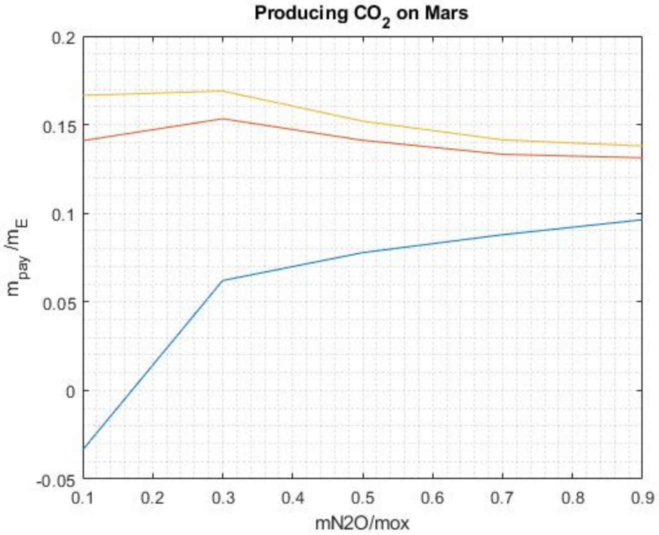

**Figure 5.12:** Maximum $\frac{m_{pay}}{m_E}$ with losses collecting $CO_2$ on Mars, varying $N_2O$ % in the oxidizer mixture for a single stage (blue), a two stage (red) and a three stage (yellow) rocket

If it's possible to collect $CO_2$ on Mars, the behaviour is different. For a single stage to orbit the pure $N_2O$ is better, while for a multistage there is a payload maximum at 70% $CO_2$ - 30% $N_2O$ (figure 5.12). If it's possible to produce even the $Mg$ on Mars, the single stage has a similar behaviour to the previous cases, while the multi-stages have a maximum for pure $CO_2$ (figure 5.13).

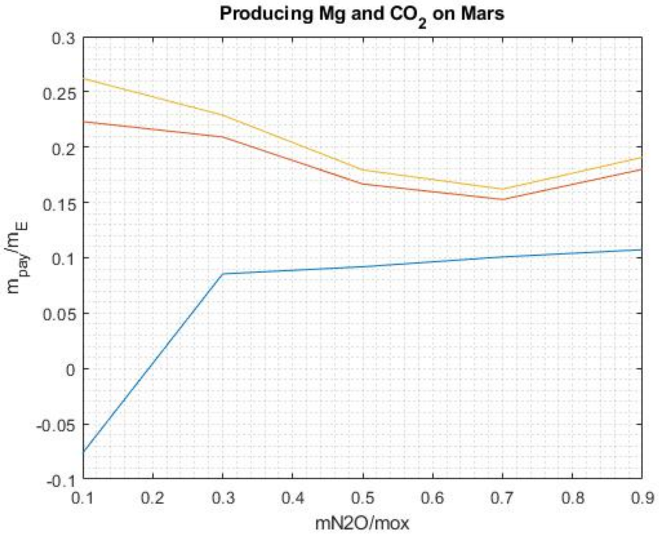

**Figure 5.13:** Maximum $\frac{m_{pay}}{m_E}$ with losses collecting the $CO_2$ and $Mg$ on Mars, varying $N_2O$ % in the oxidizer mixture for a single stage (blue), a two stage (red) and a three stage (yellow) rocket

The concentrations for $Mg$-$CO_2$-$N_2O$ to consider in the overall comparison are: pure $CO_2$, pure $N_2O$ and 70% $CO_2$ - 30% $N_2O$.

### 5.3.2 Paraffin-$Mg$-$CO_2$-$N_2O$

As for the $Mg$-$CO_2$-$N_2O$ case, it's useful to find the optimal composition of the fuel grain and of the oxidizer mixture.

#### Paraffin-$Mg$-$CO_2$-$N_2O$ without losses

For a mission without ISRU, there is a maximum of $\frac{m_{pay}}{m_E}$ using an oxidizer mixture with 90% $N_2O$. Figure 5.14 displays the behaviour for various mass percentages of magnesium in the fuel grain and mass percentages of $N_2O$ in the oxidizer mixture for a single stage rocket. The same behaviour is obtained for multi-stage rockets, leading to choose a fuel grain with 60% of $Mg$ and an oxidizer mixture with 90% $N_2O$ for a mission without ISRU.

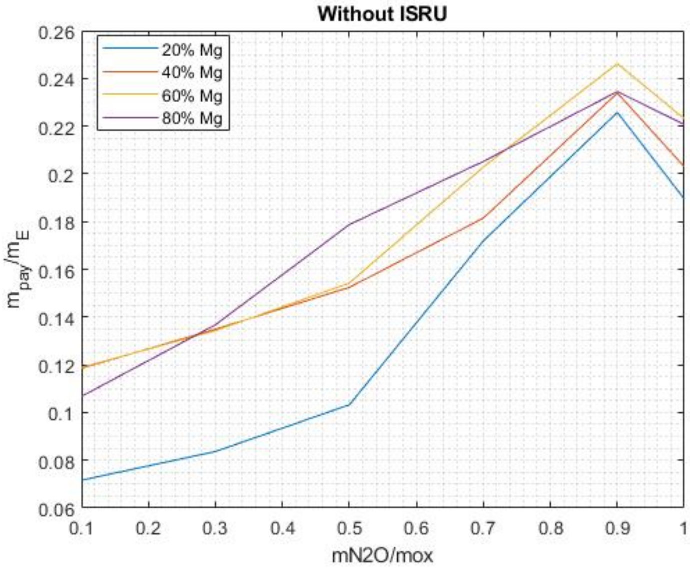

**Figure 5.14:** Maximum $\frac{m_{pay}}{m_E}$ without losses and ISRU varying $N_2O$ % in the oxidizer mixture, for a single stage rocket

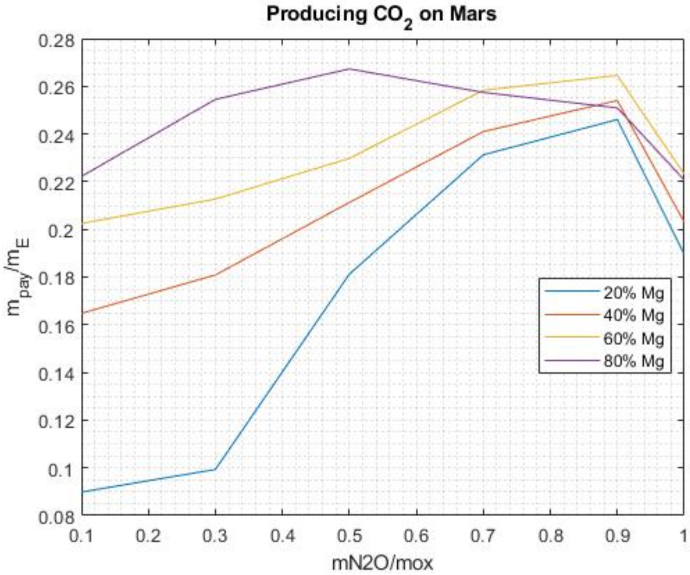

**Figure 5.15:** Maximum $\frac{m_{pay}}{m_E}$ without losses collecting $CO_2$ on Mars varying $N_2O$ % in the oxidizer mixture, for a single stage rocket

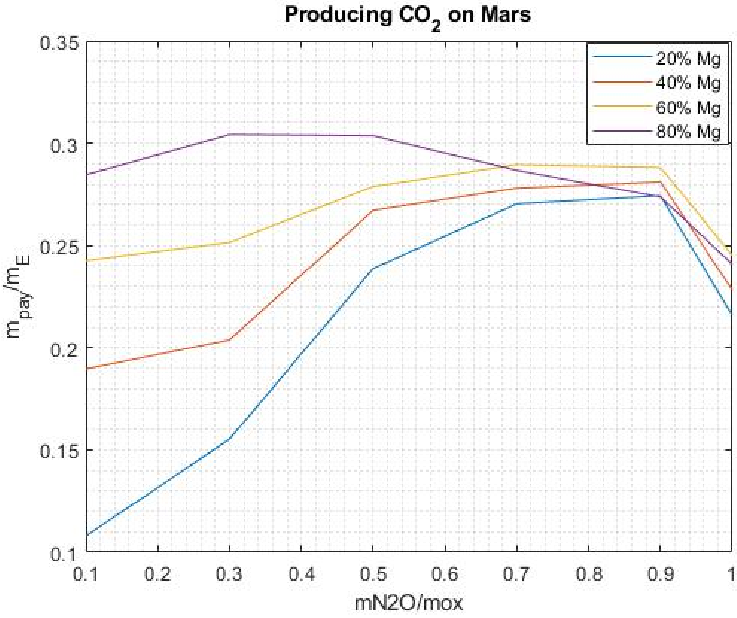

**Figure 5.16:** Maximum $\frac{m_{pay}}{m_E}$ without losses collecting $CO_2$ on Mars varying $N_2O$ % in the oxidizer mixture, for a two stage rocket

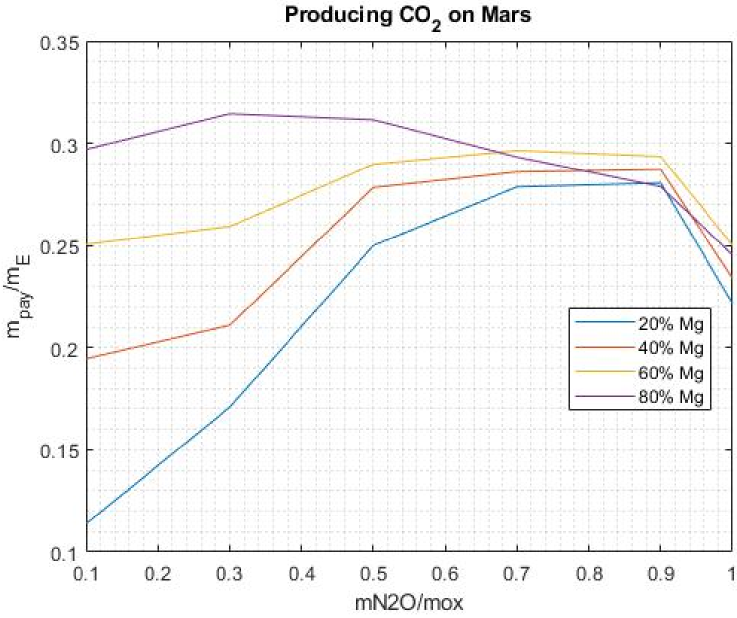

**Figure 5.17:** Maximum $\frac{m_{pay}}{m_E}$ without losses collecting $CO_2$ on Mars varying $N_2O$ % in the oxidizer mixture, for a three stage rocket

If it's possible to collect $CO_2$ on Mars, the grain and mixture chosen for the case without ISRU is comparable with a fuel grain with 80% of $Mg$ and an oxidizer mixture with 50% $N_2O$ for a single stage rocket (figure 5.15). The advantages of the latter fuel grain composition increase with the number of stages decreasing the $N_2O$ fraction to 30% as can be seen in figure 5.16 and figure 5.17. If it's even possible to produce the $Mg$ powder on Mars, the optimal composition for a single and multi-stage rocket is 80% $Mg$ fuel grain and the minimum possible mass percentage of $N_2O$ in the oxidizer mixture (at least 30% for a successful ignition as seen in Chapter 3).

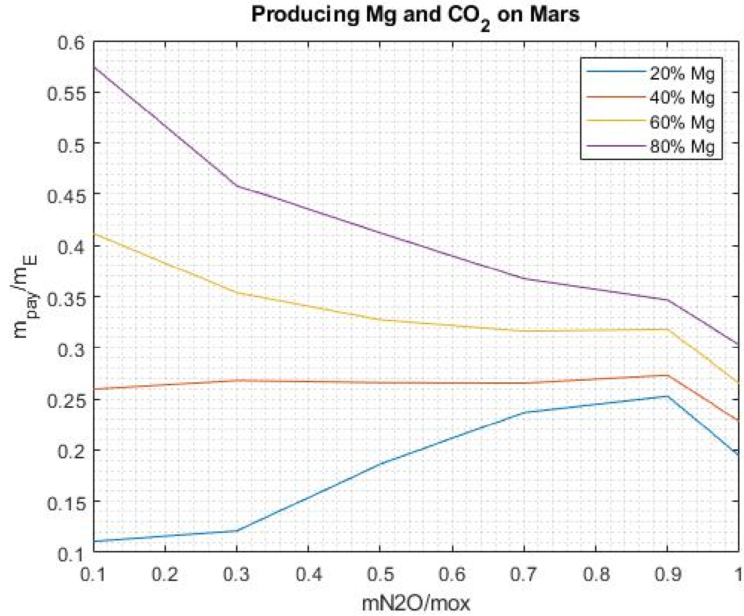

**Figure 5.18:** Maximum $\frac{m_{pay}}{m_E}$ without losses collecting $CO_2$ and $Mg$ on Mars varying $N_2O$ % in the oxidizer mixture, for a single stage rocket

### Paraffin-$Mg$-$CO_2$-$N_2O$ with losses

With maximum two phase flow losses the best choice is a fuel grain with minimum concentration of magnesium and an oxidizer mixture with 90% $N_2O$ for the case without ISRU (figure 5.19), and 70% $N_2O$ for the other two cases (figure 5.20 and figure 5.21).

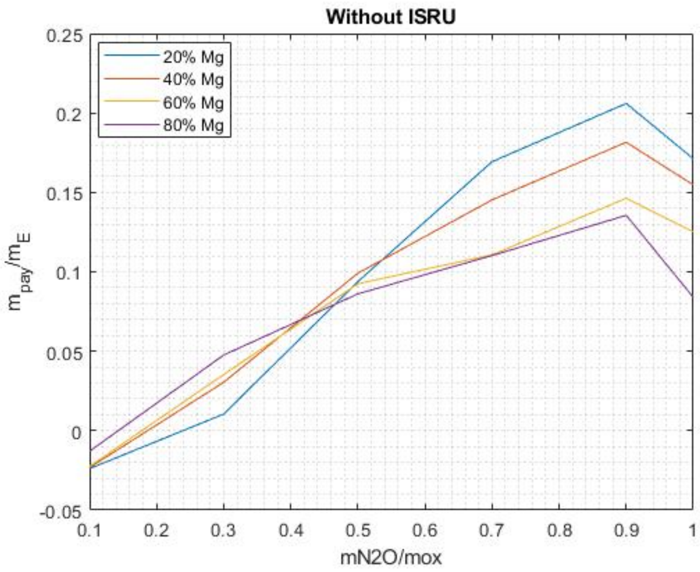

**Figure 5.19:** Maximum $\frac{m_{pay}}{m_E}$ with losses and without ISRU varying $N_2O$ % in the oxidizer mixture, for a single stage rocket

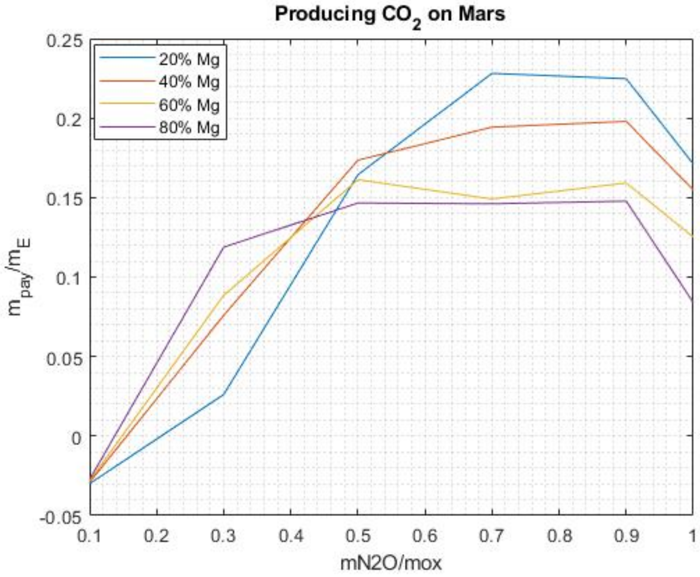

**Figure 5.20:** Maximum $\frac{m_{pay}}{m_E}$ with losses collecting $CO_2$ on Mars varying $N_2O$ % in the oxidizer mixture, for a single stage rocket

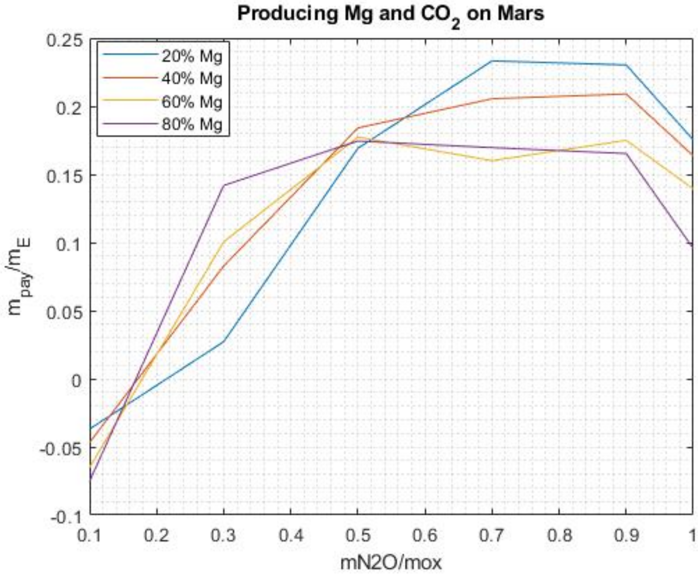

**Figure 5.21:** Maximum $\frac{m_{pay}}{m_E}$ with losses collecting $CO_2$ and $Mg$ on Mars varying $N_2O$ % in the oxidizer mixture, for a single stage rocket

The concentrations to consider in the overall comparison are: 60% $Mg$-90% $N_2O$, 80% $Mg$-30% $N_2O$ in the ideal case and 20% $Mg$-90% $N_2O$ and 20% $Mg$-70% $N_2O$ for the maximum two-phase flow losses case.

### 5.3.3 Overall Comparison

Taking into account the engines mass fractions assumed in paragraph 5.1 and the assumptions of paragraph 5.3, the different propellants combinations and engine configurations are compared in the ideal case and in the maximum two phase flow losses case for the options of table 5.1. The mass fractions and structural coefficients are evaluated at the oxidizer to fuel ratio that maximizes $\frac{m_{pay}}{m_E}$ and reported in tables. It is helpful to remember the definition of the different masses given in Chapter 4:

- $m_{pay}$ is the payload mass of the MAV;
- $m_0$ is the initial mass of the MAV on martian surface prior to its ascent;
- $m_d$ is the dry mass of the MAV defined as the sum of the structural and payload mass of the MAV;
- $m_E$ is the mass of the MAV sent from Earth.

### 5.3.4 Ideal case

In the ideal cases the effective exhaust velocities have the behaviour shown in figure 5.22, where 2010, 2030, 6010, 8070 indicate the grain and oxidizer mixtures composition for the classical hybrid configuration, $MgCO_2N_2O$ is the powder rocket with the optimal oxidizer mixture 70% $CO_2$-30% $N_2O$, and the others are $Mg$ powder rockets using pure $CO_2$, pure $N_2O$ and pure $N_2O_4$ as oxidizer. The first two numbers of the hybrid configuration name represent the mass percentage of $Mg$ in the fuel grain and the second two represent the mass percentage of $CO_2$ in the oxidizer mixture (i.e. **2010** is an hybrid with a solid grain composed of **20**% $Mg$ and (100-20)% Paraffin-wax and an oxidizer mixture composed of **10**% $CO_2$ and (100-10)% $N_2O$).

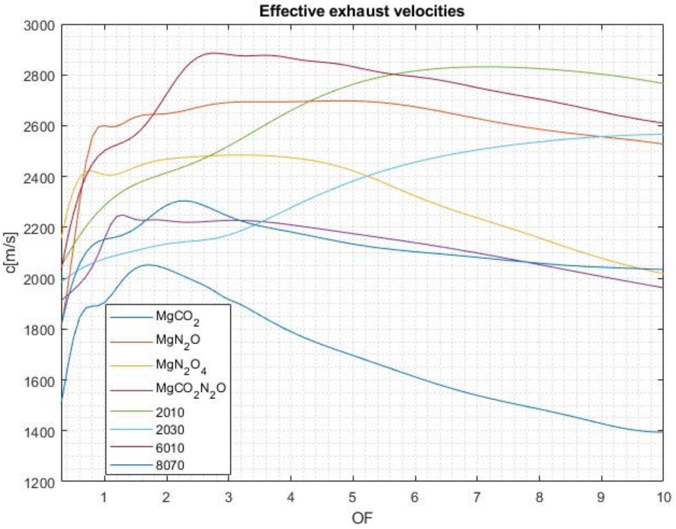

**Figure 5.22:** Effective exhaust velocities from CEA analysis

#### Without ISRU

The results for the case without ISRU are shown in table 5.2 and 5.3, where 2000, 4000, 6000 and 8000 are classical hybrids (with 20, 40, 60, 80 % $Mg$ in the paraffin based fuel grain) using pure $N_2O$ as oxidizer. From table 5.2 one can note that the most performing alternative is the $Mg$ powder rocket using pure $N_2O$ as oxidizer, with slightly higher performance than the hybrids 6000 and 8000. The increase in $\frac{m_{pay}}{m_E}$ with a two stage rocket are around 3-4%, making the single stage hybrid 6000 the better option due to its simpler configuration and comparable performance to that of the powder rocket using pure $N_2O$.

| | Single stage without ISRU | | | | | |
|---|---|---|---|---|---|---|
| | $MgN_2O$ | $MgN_2O_4$ | 2000 | 4000 | 6000 | 8000 |
| $\left(\frac{m_{pay}}{m_0}\right)_{OF_{opt}}$ | 0,121 | 0,103 | 0,093 | 0,103 | 0,116 | 0,114 |
| $\left(\frac{m_{pay}}{m_d}\right)_{OF_{opt}}$ | 0,571 | 0,577 | 0,455 | 0,483 | 0,525 | 0,528 |
| $\left(\frac{m_{pay}}{m_E}\right)_{OF_{opt}}$ | 0,138 | 0,115 | 0,103 | 0,114 | 0,131 | 0,129 |
| $OF_{opt}$ | 3,000 | 0,700 | 7,100 | 5,500 | 2,700 | 1,900 |
| $\epsilon_{OF_{opt}}$ | 0,104 | 0,084 | 0,123 | 0,123 | 0,119 | 0,115 |

**Table 5.2:** Ideal case results for a single stage, without ISRU

| | Two stage without ISRU | | | | | |
|---|---|---|---|---|---|---|
| | $MgN_2O$ | $MgN_2O_4$ | 2000 | 4000 | 6000 | 8000 |
| $\left(\frac{m_{pay}}{m_0}\right)_{OF_{opt}}$ | 0,147 | 0,128 | 0,127 | 0,134 | 0,143 | 0,140 |
| $\left(\frac{m_{pay}}{m_d}\right)_{OF_{opt}}$ | 0,575 | 0,557 | 0,490 | 0,505 | 0,529 | 0,531 |
| $\left(\frac{m_{pay}}{m_E}\right)_{OF_{opt}}$ | 0,172 | 0,146 | 0,145 | 0,154 | 0,166 | 0,163 |
| $OF_{opt}$ | 3,100 | 2,800 | 7,100 | 5,500 | 2,700 | 1,900 |
| $\epsilon_{OF_{opt}}$ | 0,127 | 0,116 | 0,151 | 0,151 | 0,148 | 0,144 |

**Table 5.3:** Ideal case results for a two stage, without ISRU

### Producing $CO_2$ on Mars

The results for a single stage producing $CO_2$ on Mars are shown in table 5.4. The most performing are the classical hybrids 6010 and 2010. Increasing the number of stages to 2, there is less differences in $\frac{m_{pay}}{m_E}$ between the alternatives, with the maximum reached by the powder rocket using $CO_2$, followed by the powder rocket with the $CO_2$-$N_2O$ mixture and the hybrid 6010. The more convenient choice for a MSR mission with the possibility of collecting $CO_2$ on Mars appears to be the classical hybrid 6010, due to its advantages over the powder rocket discussed in previous chapters, the almost identical $\frac{m_{pay}}{m_E}$ with the two stage $Mg - CO_2$ and $Mg - CO_2N_2O$ combined with a much higher $\frac{m_{pay}}{m_0}$ leading to a lighter rocket to deliver the same payload. Increasing the number of stages leads to negligible increases in $\frac{m_{pay}}{m_E}$, reducing the choice between a single stage and a two stage 6010 hybrid rocket with increases of 3.3% in $\frac{m_{pay}}{m_E}$ and 2.4% in $\frac{m_{pay}}{m_0}$ for the latter.

| | Single stage producing $CO_2$ | | | | | |
|---|---|---|---|---|---|---|
| | $MgCO_2$ | $70\%CO_2$ | 2010 | 2030 | 6010 | 8070 |
| $\left(\frac{m_{pay}}{m_0}\right)_{OF_{opt}}$ | 0,035 | 0,067 | 0,118 | 0,081 | 0,131 | 0,053 |
| $\left(\frac{m_{pay}}{m_d}\right)_{OF_{opt}}$ | 0,266 | 0,425 | 0,515 | 0,411 | 0,556 | 0,325 |
| $\left(\frac{m_{pay}}{m_E}\right)_{OF_{opt}}$ | 0,086 | 0,111 | 0,145 | 0,116 | 0,161 | 0,099 |
| $OF_{opt}$ | 1,800 | 1,300 | 7,000 | 10,1 | 2,700 | 2,300 |
| $\epsilon_{OF_{opt}}$ | 0,101 | 0,096 | 0,126 | 0,126 | 0,121 | 0,117 |

**Table 5.4:** Ideal case results for a single stage, capturing the $CO_2$ on Mars

| | Two-stage producing $CO_2$ | | | | | |
|---|---|---|---|---|---|---|
| | $MgCO_2$ | $70\%CO_2$ | 2010 | 2030 | 6010 | 8070 |
| $\left(\frac{m_{pay}}{m_0}\right)_{OF_{opt}}$ | 0,074 | 0,092 | 0,146 | 0,118 | 0,155 | 0,094 |
| $\left(\frac{m_{pay}}{m_d}\right)_{OF_{opt}}$ | 0,402 | 0,447 | 0,524 | 0,467 | 0,548 | 0,424 |
| $\left(\frac{m_{pay}}{m_E}\right)_{OF_{opt}}$ | 0,203 | 0,197 | 0,185 | 0,174 | 0,196 | 0,180 |
| $OF_{opt}$ | 2,200 | 3,900 | 7,100 | 10,2 | 2,700 | 2,400 |
| $\epsilon_{OF_{opt}}$ | 0,119 | 0,125 | 0,156 | 0,153 | 0,151 | 0,141 |

**Table 5.5:** Ideal case results for a two-stage, capturing the $CO_2$ on Mars

### Producing $CO_2$ and/or $Mg$ on Mars

If it's possible to produce $CO_2$ and $Mg$ on Mars, the most performing solution is the powder rocket using $CO_2$ as oxidizer. Due to the great increase in performances, a two stage powder rocket using $CO_2$ as oxidizer is the best solution. From the table 5.6, can be noted that for the single stage taking into account the nozzle mass, the hybrid 8070 is not the most performing between the hybrids options as seen in the previous comparison between them. This is explained by the new dependence on the mixture ratio of $\epsilon$ added by the term taking into account of the engine mass. Eq.5.6 shows how $\epsilon$ depends on the OF. The first term of $\left(\frac{K_t}{\rho_p}\right)_{eq}$ takes into account the mass of the tanks while the second is a function of $k_e$ and of the ratio between the initial mass of the stage and its propellant mass and thus of the mixture ratio $\left(\frac{m_{0j}}{m_{pj}} = \frac{1}{1-e^{-\left(\frac{\Delta V}{Nc(OF)}\right)}}\right)$.

$$\epsilon_j = \frac{K_t \frac{m_{pj}}{\rho_p} + k_e m_{0j}}{K_t \frac{m_{pj}}{\rho_p} + k_e m_{0j} + m_{pj}} = \frac{\left(\frac{K_t}{\rho_p}\right)_{eq}}{\left(\frac{K_t}{\rho_p}\right)_{eq} + 1} \rightarrow \left(\frac{K_t}{\rho_p}\right)_{eq} = \frac{K_t\,(OF)}{\rho_p\,(OF)} + \frac{k_e}{1 - e^{-\left(\frac{\Delta V}{Nc(OF)}\right)}} \tag{5.6}$$

The behaviour is modified from that represented in figure 5.23 to that shown in figure 5.24. For this case the best hybrid option is one with a 80% $Mg$ fuel grain and 50% $CO_2$ oxidizer mixture, not changing the convenience of choosing the two stage powder rocket using $CO_2$ as oxidizer.

| | Single stage producing $CO_2$ and/or $Mg$ | | | | | | | |
|---|---|---|---|---|---|---|---|---|
| | $MgCO_2$ | $MgN_2O$ | $MgN_2O_4$ | 70%$CO_2$ | 2010 | 2030 | 6010 | 8070 |
| $\left(\frac{m_{pay}}{m_0}\right)_{OF_{opt}}$ | 0,035 | 0,116 | 0,087 | 0,067 | 0,118 | 0,081 | 0,131 | 0,054 |
| $\left(\frac{m_{pay}}{m_d}\right)_{OF_{opt}}$ | 0,269 | 0,592 | 0,547 | 0,429 | 0,516 | 0,411 | 0,556 | 0,327 |
| $\left(\frac{m_{pay}}{m_E}\right)_{OF_{opt}}$ | 0,368 | 0,265 | 0,278 | 0,294 | 0,149 | 0,118 | 0,190 | 0,160 |
| $OF_{opt}$ | 1,700 | 0,800 | 0,400 | 1,200 | 6,900 | 10 | 2,600 | 2,200 |
| $\epsilon_{OF_{opt}}$ | 0,100 | 0,090 | 0,079 | 0,096 | 0,126 | 0,126 | 0,120 | 0,116 |

**Table 5.6:** Ideal case results for a single stage, producing $CO_2$ and/or $Mg$ on Mars

| | Two stage producing $CO_2$ and/or $Mg$ | | | | | | | |
|---|---|---|---|---|---|---|---|---|
| | $MgCO_2$ | $MgN_2O$ | $MgN_2O_4$ | 70%$CO_2$ | 2010 | 2030 | 6010 | 8070 |
| $\left(\frac{m_{pay}}{m_0}\right)_{OF_{opt}}$ | 0,078 | 0,138 | 0,099 | 0,072 | 0,146 | 0,118 | 0,155 | 0,095 |
| $\left(\frac{m_{pay}}{m_d}\right)_{OF_{opt}}$ | 0,420 | 0,588 | 0,538 | 0,451 | 0,524 | 0,467 | 0,548 | 0,427 |
| $\left(\frac{m_{pay}}{m_E}\right)_{OF_{opt}}$ | 0,725 | 0,316 | 0,364 | 0,492 | 0,190 | 0,178 | 0,230 | 0,281 |
| $OF_{opt}$ | 1,700 | 0,800 | 0,300 | 0,300 | 6,900 | 10,1 | 2,600 | 2,200 |
| $\epsilon_{OF_{opt}}$ | 0,116 | 0,112 | 0,095 | 0,094 | 0,156 | 0,153 | 0,151 | 0,140 |

**Table 5.7:** Ideal case results for a two-stage, producing $CO_2$ and/or $Mg$ on Mars

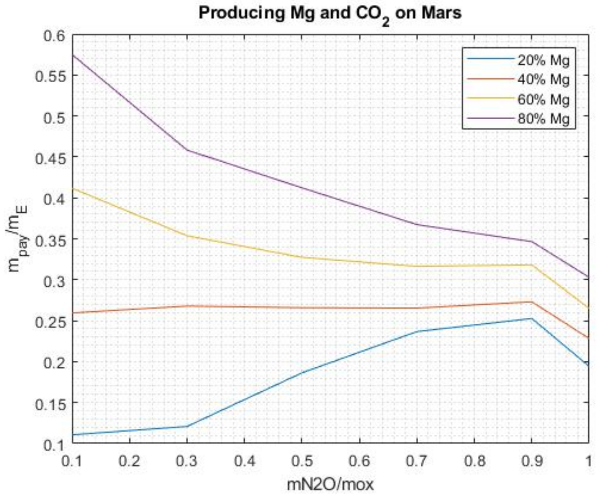

**Figure 5.23:** Maximum $\frac{m_{pay}}{m_E}$ behaviour not taking into account nozzle mass

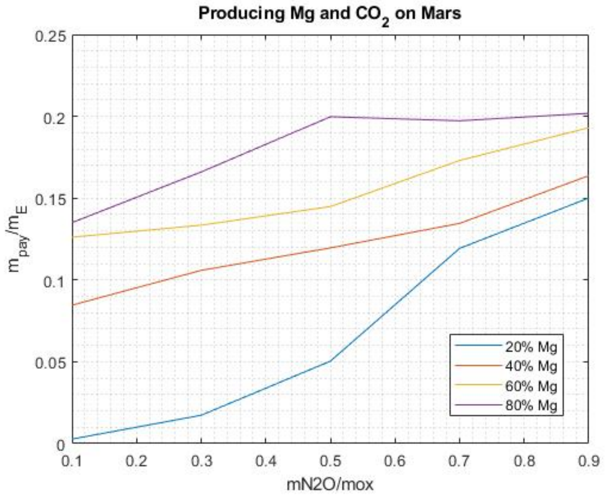

**Figure 5.24:** Maximum $\frac{m_{pay}}{m_E}$ behaviour taking into account nozzle mass

### 5.3.5 Maximum two phase flow losses case

Figure 5.25 shows the behaviour of the condensed combustion products at nozzle exit varying the OF for the propellants combinations compared. Using Eq. 5.5, the effective exhaust velocities with maximum two phase flow losses have the behaviour shown in figure 5.26. Due to the lower CCP percentages at high OF, the effective exhaust velocities are less affected by them, with the most promising configuration being the hybrid 2010.

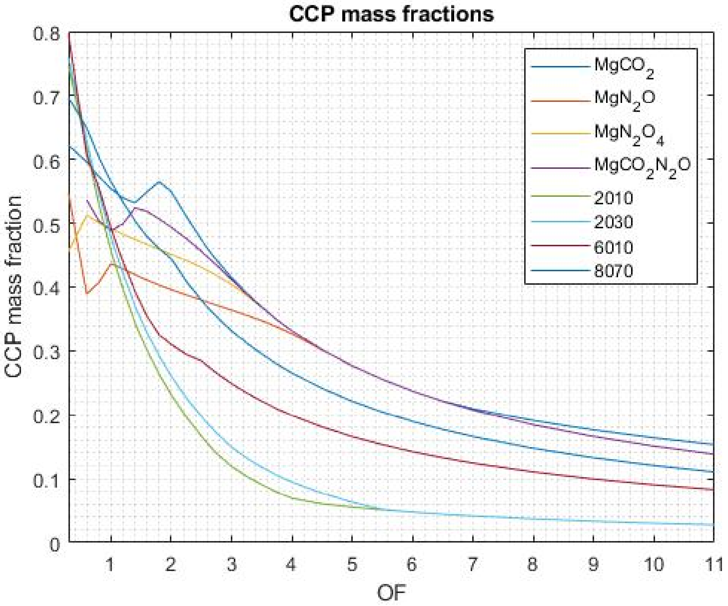

**Figure 5.25:** CCP at nozzle exit

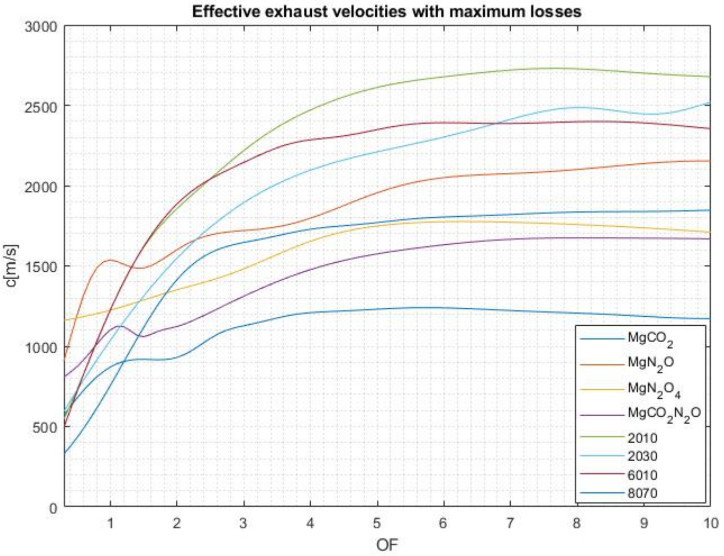

**Figure 5.26:** Exhaust velocities with maximum losses

### Without ISRU

As for the ideal case without ISRU, the $Mg$ powder rockets using pure $N_2O$ and pure $N_2O_4$ are compared with hybrids using pure $N_2O$ as oxidizer and different percentages of $Mg$. The most performing are the hybrids 2000 and 4000, with an increase in $\frac{m_{pay}}{m_E}$ of 4.5-4.6% for the two stage rocket.

| | Single stage without ISRU | | | | | |
|---|---|---|---|---|---|---|
| | $MgN_2O$ | $MgN_2O_4$ | 2000 | 4000 | 6000 | 8000 |
| $\left(\frac{m_{pay}}{m_0}\right)_{OF_{opt}}$ | 0,043 | 0,002 | 0,080 | 0,068 | 0,045 | 0,012 |
| $\left(\frac{m_{pay}}{m_d}\right)_{OF_{opt}}$ | 0,297 | 0,019 | 0,416 | 0,377 | 0,287 | 0,092 |
| $\left(\frac{m_{pay}}{m_E}\right)_{OF_{opt}}$ | 0,045 | 0,002 | 0,087 | 0,073 | 0,047 | 0,012 |
| $OF_{opt}$ | 9,800 | 6,100 | 7,1 | 6,1 | 4,7 | 5,3 |
| $\epsilon_{OF_{opt}}$ | 0,106 | 0,094 | 0,122 | 0,121 | 0,117 | 0,116 |

**Table 5.8:** Maximum two phase losses case results for a single stage, without ISRU

| | Two stage without ISRU | | | | | |
|---|---|---|---|---|---|---|
| | $MgN_2O$ | $MgN_2O_4$ | 2000 | 4000 | 6000 | 8000 |
| $\left(\frac{m_{pay}}{m_0}\right)_{OF_{opt}}$ | 0,086 | 0,051 | 0,116 | 0,107 | 0,089 | 0,064 |
| $\left(\frac{m_{pay}}{m_d}\right)_{OF_{opt}}$ | 0,432 | 0,333 | 0,469 | 0,450 | 0,409 | 0,336 |
| $\left(\frac{m_{pay}}{m_E}\right)_{OF_{opt}}$ | 0,094 | 0,054 | 0,132 | 0,119 | 0,097 | 0,069 |
| $OF_{opt}$ | 9,900 | 6,200 | 7,1 | 6,1 | 4,7 | 5,3 |
| $\epsilon_{OF_{opt}}$ | 0,123 | 0,108 | 0,149 | 0,146 | 0,141 | 0,136 |

**Table 5.9:** Maximum two phase losses case results for a two stage, without ISRU

### Producing $CO_2$ on Mars

The single stage is not sufficient for the powder rocket using $CO_2$ as oxidizer, for that using the $CO_2$-$N_2O$ mixture and for the hybrid 8070. The best performing single stage option is the hybrid 2010, with an increase of $\frac{m_{pay}}{m_E}$ by 4.3% and $\frac{m_{pay}}{m_0}$ by 3.1% for a two stage.

| | Single stage producing $CO_2$ | | | | | |
|---|---|---|---|---|---|---|
| | $MgCO_2$ | $70\%CO_2$ | 2010 | 2030 | 6010 | 8070 |
| $\left(\frac{m_{pay}}{m_0}\right)_{OF_{opt}}$ | -0,078 | -0,028 | 0,105 | 0,079 | 0,062 | -0,020 |
| $\left(\frac{m_{pay}}{m_d}\right)_{OF_{opt}}$ | -113,364 | -0,334 | 0,483 | 0,405 | 0,353 | -0,191 |
| $\left(\frac{m_{pay}}{m_E}\right)_{OF_{opt}}$ | -0,092 | -0,060 | 0,127 | 0,113 | 0,071 | -0,045 |
| $OF_{opt}$ | 0,300 | 7,400 | 7,600 | 10,5 | 5,900 | 10,400 |
| $\epsilon_{OF_{opt}}$ | 0,073 | 0,107 | 0,125 | 0,126 | 0,121 | 0,123 |

**Table 5.10:** Maximum two phase losses case results for a single stage, capturing the $CO_2$ on Mars

| | Two stage producing $CO_2$ | | | | | |
|---|---|---|---|---|---|---|
| | $MgCO_2$ | $70\%CO_2$ | 2010 | 2030 | 6010 | 8070 |
| $\left(\frac{m_{pay}}{m_0}\right)_{OF_{opt}}$ | 0,007 | 0,036 | 0,136 | 0,117 | 0,102 | 0,046 |
| $\left(\frac{m_{pay}}{m_d}\right)_{OF_{opt}}$ | 0,055 | 0,237 | 0,506 | 0,464 | 0,436 | 0,254 |
| $\left(\frac{m_{pay}}{m_E}\right)_{OF_{opt}}$ | 0,028 | 0,084 | 0,170 | 0,172 | 0,123 | 0,106 |
| $OF_{opt}$ | 5,900 | 9,300 | 7,600 | 10,5 | 8,300 | 10,600 |
| $\epsilon_{OF_{opt}}$ | 0,114 | 0,121 | 0,154 | 0,153 | 0,147 | 0,141 |

**Table 5.11:** Maximum two phase losses case results for a two-stage, capturing the $CO_2$ on Mars

### Producing $CO_2$ and $Mg$ on Mars

As for the previous case the single stage is not sufficient for the powder rocket using $CO_2$ as oxidizer, for that using the $CO_2$-$N_2O$ mixture and for the hybrid 8070. The hybrid 2010 remains the best performing single stage option with an increase of $\frac{m_{pay}}{m_E}$ by 4.4% and $\frac{m_{pay}}{m_0}$ by 3.1% for a two stage.

| | Single stage producing $CO_2$ and $Mg$ | | | | | | | |
|---|---|---|---|---|---|---|---|---|
| | $MgCO_2$ | $MgN_2O$ | $MgN_2O_4$ | $70\%CO_2$ | 2010 | 2030 | 6010 | 8070 |
| $\left(\frac{m_{pay}}{m_0}\right)_{OF_{opt}}$ | -0,080 | 0,043 | 0,002 | -0,028 | 0,105 | 0,079 | 0,062 | -0,020 |
| $\left(\frac{m_{pay}}{m_d}\right)_{OF_{opt}}$ | -2,301 | 0,297 | 0,019 | -0,332 | 0,483 | 0,405 | 0,353 | -0,191 |
| $\left(\frac{m_{pay}}{m_E}\right)_{OF_{opt}}$ | -0,697 | 0,049 | 0,002 | -0,078 | 0,130 | 0,115 | 0,078 | -0,052 |
| $OF_{opt}$ | 5,600 | 9,800 | 6,100 | 7,800 | 7,600 | 10,5 | 5,800 | 10,500 |
| $\epsilon_{OF_{opt}}$ | 0,106 | 0,106 | 0,094 | 0,108 | 0,125 | 0,126 | 0,121 | 0,123 |

**Table 5.12:** Maximum two phase losses case results for a single stage, producing $CO_2$ and $Mg$ on Mars

| | Two stage producing $CO_2$ and $Mg$ | | | | | | | |
|---|---|---|---|---|---|---|---|---|
| | $MgCO_2$ | $MgN_2O$ | $MgN_2O_4$ | $70\%CO_2$ | 2010 | 2030 | 6010 | 8070 |
| $\left(\frac{m_{pay}}{m_0}\right)_{OF_{opt}}$ | 0,007 | 0,086 | 0,051 | 0,036 | 0,136 | 0,117 | 0,102 | 0,046 |
| $\left(\frac{m_{pay}}{m_d}\right)_{OF_{opt}}$ | 0,056 | 0,431 | 0,332 | 0,240 | 0,506 | 0,464 | 0,438 | 0,254 |
| $\left(\frac{m_{pay}}{m_E}\right)_{OF_{opt}}$ | 0,059 | 0,102 | 0,062 | 0,107 | 0,174 | 0,175 | 0,133 | 0,123 |
| $OF_{opt}$ | 5,600 | 9,700 | 5,800 | 7,500 | 7,600 | 10,5 | 5,800 | 10,500 |
| $\epsilon_{OF_{opt}}$ | 0,114 | 0,123 | 0,107 | 0,120 | 0,154 | 0,153 | 0,145 | 0,141 |

**Table 5.13:** Maximum two phase losses case results for a two-stage, producing $CO_2$ and $Mg$ on Mars

# Chapter 6

# Comparison conclusions

The most performing alternatives for the various ISRU options found in the previous Chapter are reported in table 6.1 and 6.2 with the most performing configurations without ISRU for comparison.

| | Ideal | | | Maximum two-phase flow losses | | |
|---|---|---|---|---|---|---|
| | Without ISRU | Producing | | Without ISRU | Producing | |
| | | $CO_2$ | $CO_2$ & $Mg$ | | $CO_2$ | $CO_2$ & $Mg$ |
| | 6000 | 6010 | $MgCO_2$ | 2000 | 2010 | 2010 |
| $\left(\frac{m_{pay}}{m_0}\right)_{OF_{opt}}$ | 0,116 | 0,131 | 0,035 | 0,08 | 0,105 | 0,105 |
| $\left(\frac{m_{pay}}{m_d}\right)_{OF_{opt}}$ | 0,525 | 0,556 | 0,269 | 0,416 | 0,483 | 0,483 |
| $\left(\frac{m_{pay}}{m_E}\right)_{OF_{opt}}$ | 0,131 | 0,161 | 0,368 | 0,087 | 0,127 | 0,13 |
| $OF_{opt}$ | 2,7 | 2,7 | 1,7 | 7,1 | 7,6 | 7,6 |
| $\epsilon_{OF_{opt}}$ | 0,119 | 0,121 | 0,1 | 0,122 | 0,125 | 0,125 |
| $c\left(OF_{opt}\right)\ \left[\frac{m}{s}\right]$ | 2759 | 2885 | 2052 | 2532 | 2730 | 2730 |

**Table 6.1:** Single stage results

| | Ideal | | | Maximum two-phase flow losses | | |
|---|---|---|---|---|---|---|
| | Without | Producing | | Without | Producing | |
| | ISRU | $CO_2$ | $CO_2$ & $Mg$ | ISRU | $CO_2$ | $CO_2$ & $Mg$ |
| | 6000 | 6010 | $MgCO_2$ | 2000 | 2010 | 2010 |
| $\left(\frac{m_{pay}}{m_0}\right)_{OF_{opt}}$ | 0,143 | 0,155 | 0,078 | 0,116 | 0,136 | 0,136 |
| $\left(\frac{m_{pay}}{m_d}\right)_{OF_{opt}}$ | 0,529 | 0,548 | 0,42 | 0,469 | 0,506 | 0,506 |
| $\left(\frac{m_{pay}}{m_E}\right)_{OF_{opt}}$ | 0,166 | 0,196 | 0,725 | 0,132 | 0,17 | 0,174 |
| $OF_{opt}$ | 2,7 | 2,7 | 1,7 | 7,1 | 7,6 | 7,6 |
| $\epsilon_{OF_{opt}}$ | 0,148 | 0,151 | 0,116 | 0,149 | 0,154 | 0,154 |
| $c\left(OF_{opt}\right)\ \left[\frac{m}{s}\right]$ | 2759 | 2885 | 2052 | 2532 | 2730 | 2730 |

**Table 6.2:** Two stage results

All the calculations of the previous chapters concerned only the mass of the MAV and ignored that of the systems needed to produce the propellant.

A case with ISRU is convenient over one without it if the following relation is satisfied:

$$m_{pay_{ISRU}} - m_{pay_{WOISRU}} > m_{pps} \tag{6.1}$$

Where $m_{pay_{ISRU}}$ is the payload mass of the MAV for a mission with ISRU, $m_{pay_{WOISRU}}$ is the payload mass of the MAV for a mission without ISRU and $m_{pps}$ is the mass of the propellant production system. Dividing each member of 6.1 by a chosen mass of the MAV sent from Earth $m_E$, it's possible to find a limit for the mass fraction of the propellant production system that makes the ISRU option convenient:

$$\left(\frac{m_{pay_{ISRU}}}{m_E}\right) - \left(\frac{m_{pay_{WOISRU}}}{m_E}\right) > \frac{m_{pps}}{m_E} \tag{6.2}$$

### Propellant production system mass fraction

The propellant production system is composed of a power system and a propellant acquisition and transformation (*at*) system. Following the procedure used by Shafirovich[31], it is possible to estimate the masses of these two subsystems knowing the acquisition and transformation time, the propellant mass rate production per kg of the *at* system and the specific powers of the power system and of the *at* system. Known the *at* time, the *at* system mass $m_{at}$ is defined as:

$$m_{at} = \frac{1}{yt_{at}} m_{p_{pr}} \tag{6.3}$$

Where $y$ $\left[\frac{kg}{kg day}\right]$ is the propellant mass rate production per kg of the at system, $t_{at}$ is the *at* time and $m_{p_{pr}}$ is the mass of propellant produced. The power $P$ needed by the acquisition and transformation system is proportional to its mass and defined as:

$$P = P_{at} m_{at} \tag{6.4}$$

Where $P_{at}$ $\left[\frac{W}{kg}\right]$ is the specific power required per kg of the *at* system. It is possible to estimate the mass of the power system by equating its power with that required by the *at* system:

$$P = P_{ps} m_{ps} = P_{at} m_{at} \rightarrow m_{ps} = \frac{P_{at}}{P_{ps}} m_{at} \tag{6.5}$$

Where $m_{ps}$ is the mass of the power system and $P_{ps}$ $\left[\frac{W}{kg}\right]$ is its specific power. The mass of the propellant production system is the sum of $m_{at}$ and $m_{ps}$:

$$m_{pps} = m_{at} + m_{ps} = m_{at} \left(1 + \frac{P_{at}}{P_{ps}}\right) = \frac{1}{y t_{at}} \left(1 + \frac{P_{at}}{P_{ps}}\right) m_{p_{pr}} \tag{6.6}$$

The propellant production system mass fraction $\frac{m_{pps}}{m_E}$ can be obtained as a function of mass fractions already estimated in previous Chapters and dividing Eq.6.6 by $m_0$:

$$\frac{m_{pps}}{m_E} = \frac{m_{pps}}{m_0} \frac{m_0}{m_{pay}} \frac{m_{pay}}{m_E} \tag{6.7}$$

### Propellant production system mass fraction collecting $CO_2$

Despite the higher limits for $\frac{m_{pps}}{m_E}$, a MSR mission involving the production of $Mg$ powder on Mars seems too complex to accomplish compared to one involving only the production of $CO_2$.

Collecting only the $CO_2$ on Mars, Eq. 6.6 becomes:

$$m_{pps} = \frac{1}{y t_{at}} \left(1 + \frac{P_{at}}{P_{ps}}\right) m_{CO_2} = \frac{1}{y t_{at}} \left(1 + \frac{P_{at}}{P_{ps}}\right) \frac{OF}{1+OF} \chi_{CO_2} m_p \tag{6.8}$$

Where $\chi_{CO_2}$ is the mass fraction of the $CO_2$ in the oxidizer mixture and $m_p$ is the propellant mass. Remembering that for a multistage using stages with same properties $m_p = \left(1 - e^{-\frac{\Delta V}{Nc}}\right) m_0 \sum_{j=1}^{N} \lambda^{j-1}$ (Eq. 4.30), Eq.6.8 becomes:

$$\frac{m_{pps}}{m_0} = \frac{1}{y t_{at}} \left(1 + \frac{P_{at}}{P_{ps}}\right) \frac{OF}{1+OF} \chi_{CO_2} \left(1 - e^{-\frac{\Delta V}{Nc}}\right) \sum_{j=1}^{N} \lambda^{j-1} \tag{6.9}$$

Where N is the number of stages and $\lambda = \frac{m_{pay_j}}{m_{0_j}} = \left(\frac{m_{pay}}{m_0}\right)^{\frac{1}{N}}$.

Estimating $m_{pps}$ for a martian $Mg$-$CO_2$ hopper producing liquid $CO_2$ on Mars, Shafirovich[31] assumes $y = 0{,}1\ \frac{kg}{daykg}$ for a sorption compressor requiring a maximum $P_{at} = 15\ \frac{W}{kg}$ and assuming $P_{ps} = 0.9961^{t_{at}} 16.7\ \frac{W}{kg}$ for the specific power of the solar panels taking into account their degradation with time ($t_{at}$ expressed in days). Assuming a round trip mission using only Hohmann transfers, the wait time on the surface of Mars is 454 days[32]. Choosing $t_{at} = 454\ days$, the properties of the propellant production system and the data estimated in the previous Chapter, one can calculate $\frac{m_{pps}}{m_E}$ and verify the convenience of $CO_2$ production with rel.6.2 for the analyzed cases.

### Ideal case

In the ideal case the best performing alternatives are:

- the hybrid 6010 (60% Mg-(40%)paraffin solid fuel grain, using 10% $CO_2$-(90%)$N_2O$ mixture as oxidizer) for the case with the collection of $CO_2$ on Mars;
- the $Mg$ powder rocket using pure $CO_2$ as oxidizer for the case collecting $CO_2$ and $Mg$ on Mars;
- the hybrid 6000 (60% Mg-(40%)paraffin solid fuel grain, using pure $N_2O$ as oxidizer) for the case without ISRU.

The case with the collection of $CO_2$ on Mars has a limit for the propellant production system mass fraction $\frac{m_{pps}}{m_E}$ of 3% for the single and for the two stage. With the assumption of the previous paragraph, the value of $\frac{m_{pps}}{m_E}$ is 0.95 % for the single stage and 0.92 % for the two stage, resulting within the limit in both cases.

Clearly the case with the production of $Mg$ and $CO_2$ on Mars has the higher $\frac{m_{pay}}{m_E}$. As a consequence the limit for the propellant production system mass fraction is higher. $\frac{m_{pps}}{m_E}$ has to be less than 23.7% for a single stage and 55.9% for a two stage.

### Maximum two phase flow losses case

In the case with maximum two phase flow losses the best performing alternatives are:

- the hybrid 2010 (20% Mg-(80%)paraffin solid fuel grain, using 10% $CO_2$-(90%)$N_2O$ mixture as oxidizer) for the case with the collection of $CO_2$ and for the case with the production of $Mg$ and $CO_2$ on Mars;
- the hybrid 2000 (20% Mg-(80%)paraffin solid fuel grain, using pure $N_2O$ as oxidizer) for the case without ISRU.

The case with the collection of $CO_2$ on Mars has a limit for the propellant production system mass fraction $\frac{m_{pps}}{m_E}$ of 4% for the single stage and of 3.8% for the two stage. With the assumption of the previous paragraph, the value of $\frac{m_{pps}}{m_E}$ is 1.16 % for the single stage and 1.12 % for the two stage, resulting within the limit in both cases. The case with the production of $Mg$ and $CO_2$ on Mars with maximum two phase flow losses does not have a particularly high $\frac{m_{pay}}{m_E}$ due to the low percentage of $Mg$ and $CO_2$ of the propellants. As a consequence the limits for $\frac{m_{pps}}{m_E}$ are 4.3% for the single stage and 4.2% for the two stage, comparable with the limits of the previous case.

### 6.0.1 Conclusions

For the obtained results, one can note that collecting $CO_2$ on Mars is convenient in the ideal case and in the maximum two phase flow losses case. The production of $CO_2$ and $Mg$ on Mars seems particularly promising for a two stage $Mg$-$CO_2$ powder rocket MAV due to its $\frac{m_{pay}}{m_E}$ outclassing that of all the alternatives and the relative high margin of 55.9% for $\frac{m_{pps}}{m_E}$.

Considering Szabo's [8] experiments conclusions seen in Chapter 2, the specific impulse of the powder rocket engine can be considered closer to the ideal one than to that with maximum two phase flow losses. Due to the lower condensed combustion products mass fraction, the same conclusion seems reasonable for the hybrid configurations leading to the choice of the hybrid 6010, for the missions with the collection of $CO_2$ from martian atmosphere, and of the powder Mg-$CO_2$ rocket, for the more complex ISRU case involving even the production of magnesium powder on Mars.

The low value of the optimal OFs found for the ideal cases are associated to high condensed combustion products mass fractions (see figure 6.1).

Even if the condensed combustion products do not reduce too much the specific impulse, an excessive deposition of magnesium oxide and carbon in the combustion chamber and nozzle could be problematic. It can lead to instability and inefficiency as seen in Chapter 2 for the powder $Mg$-$CO_2$ engine, and to the gradual obstruction of the nozzle throat as seen in Chapter 3 for the Paraffin wax -$Mg$-$CO_2$-$N_2O$ hybrid. It is possible to reduce the CCP mass fraction increasing the OF. Moving away from the optimal OF reduces the margin for $\frac{m_{pps}}{m_E}$ until the option with ISRU is no more convenient.

The OF limits for the convenience of collecting $CO_2$ for a 6010 hybrid MAV over the 6000 hybrid without ISRU option, are defined by rel. 6.2 and displayed in figure 6.2 and 6.3 for a single and a two stage rocket.

For a Mars sample return mission the more promising, and feasible in the near term, propulsion option involving $Mg$-$CO_2$ combustion is the hybrid 6010 with $CO_2$ collection. Its CCP mass fraction is around 27% at the optimal OF=2.7

and, if it is not acceptable, can be reduced up to around 15% for a single stage, increasing OF to 5.6, and up to around 13% for a two stage, increasing OF to 6.6.

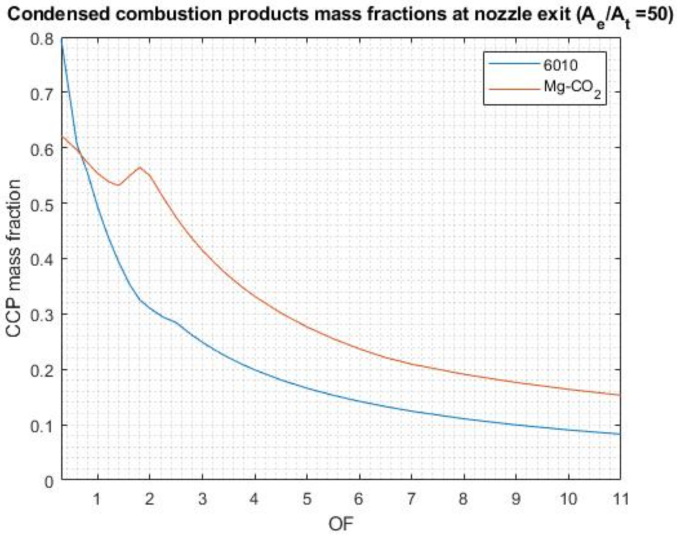

**Figure 6.1:** Condensed combustion products mass fractions at nozzle exit for the powder $Mg$-$CO_2$ engine and for the Paraffin wax -$Mg$-$CO_2$-$N_2O$ hybrid 6010

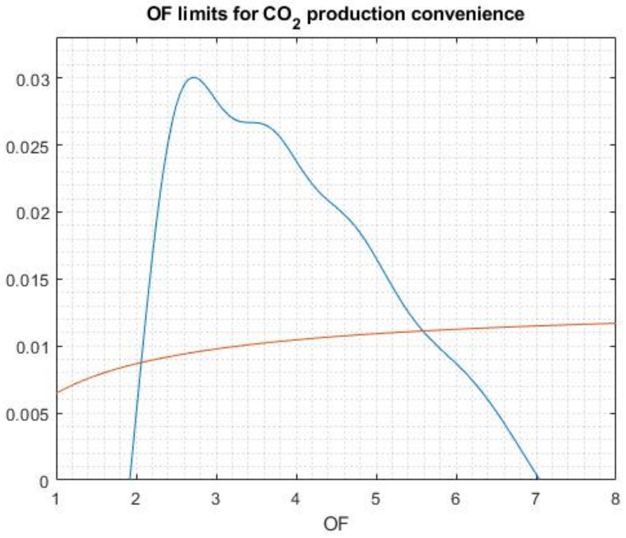

**Figure 6.2:** $\left(\frac{m_{pay_{ISRU}}}{m_E}\right) - \left(\frac{m_{pay_{WOISRU}}}{m_E}\right)$ (blue), $\frac{m_{pps}}{m_E}$ (red) for a single stage 6010 hybrid

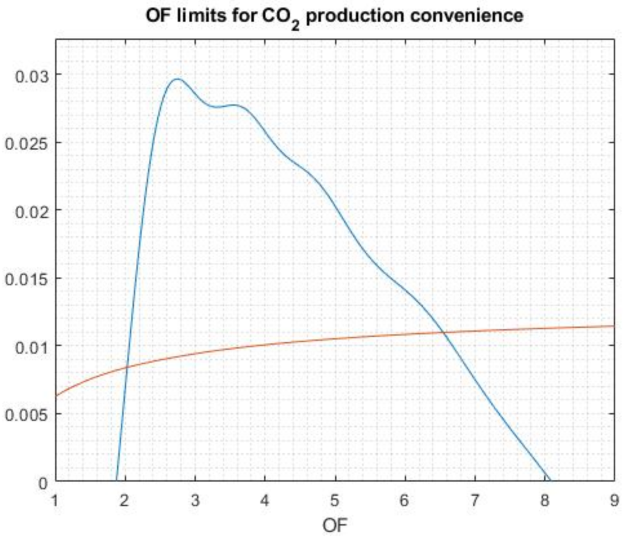

**Figure 6.3:** $\left(\frac{m_{pay_{ISRU}}}{m_E}\right) - \left(\frac{m_{pay_{WOISRU}}}{m_E}\right)$ (blue), $\frac{m_{pps}}{m_E}$ (red) for a two stage 6010 hybrid

# Bibliography

[1] Roland Martinez, Kandyce E Goodliff, and Ryan J Whitley. «ISECG global exploration roadmap: A stepwise approach to deep space exploration». In: *AIAA SPACE 2013 Conference and Exposition*. 2013, p. 5504 (cit. on p. 1).

[2] M. H. Carr. *The Geology of the Terrestrial Planets*. Washington, D.C.: NASA, Scientific and Technical Information Branch, 1984 (cit. on pp. 1, 8, 47).

[3] Litchford R.J. Foote J.P. *Powdered Magnesium-Carbon Dioxide Rocket Combustion Technology for In Situ Mars Propulsion*. Tech. rep. M-1203,NASA/TP-2007-215077. Marshall Space Flight Center Huntsville: NASA, Sept. 2007 (cit. on p. 1).

[4] Evgeny Ya Shafirovich and Udo I Goldshleger. «Comparison of Potential Fuels for Martian Rockets Using CO». In: *Journal of Propulsion and Power* 13.3 (1997), pp. 395–397 (cit. on pp. 1–3).

[5] U. I. Goldshleger E. Ya. Shafirovich A. A. Shiryaev. «Magnesium and carbon dioxide: A rocket propellant for Mars missions». In: *Journal of propulsion and power* 9.2 (1993), pp. 197–203. ISSN: 0748-4658 (cit. on pp. 1, 4, 5, 12, 13).

[6] John Wickman. «In-situ mars rocket and jet engines burning carbon dioxide». In: *35th Joint Propulsion Conference and Exhibit*. 1999, p. 2409 (cit. on pp. 1, 4, 8).

[7] Ozan Kara, Hakkı Karakaş, and M. Arif Karabeyoğlu. «Hybrid rockets with mixed N2O/CO2 oxidizers for Mars Ascent Vehicles». In: *Acta Astronautica* 175 (2020), pp. 254–267. ISSN: 0094-5765. DOI: `https://doi.org/10.1016/j.actaastro.2020.05.060`. URL: `https://www.sciencedirect.com/science/article/pii/S009457652030343X` (cit. on pp. 1, 28).

[8] James Szabo, Timothy Miller, John Herr, and Jon Peters. «Magnesium Bipropellant Rockets for Martian Ascent Vehicles». In: *47th AIAA/ASME/SAE/ASEE Joint Propulsion Conference & Exhibit*. 2011, p. 5834 (cit. on pp. 5, 11, 73).

[9] Chao Li, Chunbo Hu, Xiaofei Zhu, Jiaming Hu, Yue Li, and Xu Hu. «Experimental study on the thrust modulation performance of powdered magnesium and CO2 bipropellant engine». In: *Acta Astronautica* 147 (2018), pp. 403–411. ISSN: 0094-5765. DOI: `https://doi.org/10.1016/j.actaastro.2018.03.029`. URL: `https://www.sciencedirect.com/science/article/pii/S009457651731901X` (cit. on pp. 5, 7).

[10] Yue Li, Chunbo Hu, Xiaofei Zhu, Jiaming Hu, Xu Hu, Chao Li, and Yupeng Cai. «Experimental study on combustion characteristics of powder magnesium and carbon dioxide in rocket engine». In: *Acta Astronautica* 155 (2019), pp. 334–349. ISSN: 0094-5765. DOI: `https://doi.org/10.1016/j.actaastro.2018.11.006`. URL: `https://www.sciencedirect.com/science/article/pii/S009457651831138X` (cit. on pp. 5–7, 9–11, 13–16).

[11] Jiaming Hu, Chunbo Hu, Yanhong Che, Xiaofei Zhu, Jiangang Yang, Mengzhe Li, and Chao Li. «Experimental study on the working performance of powdered magnesium and liquid carbon dioxide bipropellant rocket engine for Mars missions». In: *Acta Astronautica* 184 (2021), pp. 274–285. ISSN: 0094-5765. DOI: `https://doi.org/10.1016/j.actaastro.2021.04.025`. URL: `https://www.sciencedirect.com/science/article/pii/S0094576521001715` (cit. on pp. 5–7, 9, 10, 16).

[12] Kewu Zhu, S. Madhusudana Rao, Chi-Hwa Wang, and Sankaran Sundaresan. «Electrical capacitance tomography measurements on vertical and inclined pneumatic conveying of granular solids». In: *Chemical Engineering Science* 58.18 (2003), pp. 4225–4245. ISSN: 0009-2509. DOI: `https://doi.org/10.1016/S0009-2509(03)00306-3`. URL: `https://www.sciencedirect.com/science/article/pii/S0009250903003063` (cit. on p. 7).

[13] Benjamin Legrand, Evgeny Shafirovich, Michaël Marion, Christian Chauveau, and Iskender Gökalp. «Ignition and combustion of levitated magnesium particles in carbon dioxide». In: *Symposium (International) on Combustion* 27.2 (1998), pp. 2413–2419. ISSN: 0082-0784. DOI: `https://doi.org/10.1016/S0082-0784(98)80093-3`. URL: `https://www.sciencedirect.com/science/article/pii/S0082078498800933` (cit. on p. 9).

[14] Bonnie J McBride. *Computer program for calculation of complex chemical equilibrium compositions and applications.* Vol. 2. NASA Lewis Research Center, 1996 (cit. on pp. 16, 17, 27, 29, 44).

[15] Sanford Gordon and Bonnie J McBride. *Computer program for calculation of complex chemical equilibrium compositions and applications. Part 1: Analysis.* Tech. rep. 1994 (cit. on pp. 16, 17, 27, 29, 44).

[16] Ozan Kara and Arif Karabeyoglu. «Hybrid Propulsion System: Novel Propellant Design for Mars Ascent Vehicles». In: *Propulsion.* Ed. by Kazuo Matsuuchi and Hiroaki Hasegawa. Rijeka: IntechOpen, 2021. Chap. 2. DOI: `10.5772/intechopen.96686`. URL: `https://doi.org/10.5772/intechopen.96686` (cit. on pp. 18, 19, 28, 29).

[17] G.N. Henry, R.W. Humble, W.J. Larson, United States. Department of Defense, United States. National Aeronautics, and Space Administration. *Space Propulsion Analysis and Design.* College custom series. McGraw-Hill, 1995. ISBN: 9780070313293. URL: `https://books.google.it/books?id=7OmMKQAACAAJ` (cit. on pp. 18, 21, 22, 42, 45, 48).

[18] G. Marxman and M. Gilbert. «Turbulent boundary layer combustion in the hybrid rocket». In: *Symposium (International) on Combustion* 9.1 (1963), pp. 371–383. ISSN: 0082-0784. DOI: `https://doi.org/10.1016/S0082-0784(63)80046-6`. URL: `https://www.sciencedirect.com/science/article/pii/S0082078463800466` (cit. on pp. 20, 21).

[19] M. Chiaverini. «Review of solid-fuel regression rate behavior in classical and nonclassical hybrid rocket motors». In: *Fundamentals of Hybrid Rocket Combustion and Propulsion* 218 (2007) (cit. on pp. 20–23).

[20] G.A. Marxman, C.E. Wooldridge, and R.J. Muzzy. «Fundamentals of Hybrid Boundary-Layer Combustion». In: *Heterogeneous Combustion.* Ed. by Hans G. Wolfhard, Irvin Glassman, and Leon Green. Vol. 15. Progress in Astronautics and Rocketry. Elsevier, 1964, pp. 485–522. DOI: `https://doi.org/10.1016/B978-1-4832-2730-6.50025-7`. URL: `https://www.sciencedirect.com/science/article/pii/B9781483227306500257` (cit. on p. 22).

[21] Arif Karabeyoglu, D. Altman, and B. Cantwell. «Combustion of Liquefying Hybrid Propellants: Part 1, General Theory». In: *Journal of Propulsion and Power - J PROPUL POWER* 18 (May 2002). DOI: `10.2514/2.5975` (cit. on pp. 22, 23).

[22] M. Karabeyoglu, B. Cantwell, and D. Altman. «Development and testing of paraffin-based hybrid rocket fuels». In: *37th Joint Propulsion Conference and Exhibit.* DOI: `10.2514/6.2001-4503`. eprint: `https://arc.aiaa.org/doi/pdf/10.2514/6.2001-4503`. URL: `https://arc.aiaa.org/doi/abs/10.2514/6.2001-4503` (cit. on pp. 24, 25).

[23] Arif Karabeyoglu, Brian Cantwell, and Jose Stevens. «Evaluation of the Homologous Series of Normal Alkanes as Hybrid Rocket Fuels». In: *41st AIAA/ASME/SAE/ASEE Joint Propulsion Conference &amp; Exhibit.* DOI: `10.2514/6.2005-3908`. eprint: `https://arc.aiaa.org/doi/pdf/10.2514/6.2005-3908`. URL: `https://arc.aiaa.org/doi/abs/10.2514/6.2005-3908` (cit. on pp. 24, 25).

[24] Arif Karabeyoglu. «Mixtures of Nitrous Oxide, Carbon Dioxide and Oxygen as Oxidizers for Mars Applications». In: *46th AIAA/ASME/SAE/ASEE Joint Propulsion Conference &amp; Exhibit*. DOI: `10.2514/6.2010-6712`. eprint: `https://arc.aiaa.org/doi/pdf/10.2514/6.2010-6712`. URL: `https://arc.aiaa.org/doi/abs/10.2514/6.2010-6712` (cit. on pp. 26, 28).

[25] Ozan Kara and Arif Karabeyoglu. «Ignition Capability of CO 2 in Hybrid Rockets for Mars Ascent Vehicles». PhD thesis. Mar. 2021. DOI: `10.13140/RG.2.2.27962.72641` (cit. on pp. 29–34).

[26] M. Arif Karabeyoglu, Brian J. Cantwell, and Greg Zilliac. «Development of Scalable Space-Time Averaged Regression Rate Expressions for Hybrid Rockets». In: *Journal of Propulsion and Power* 23.4 (2007), pp. 737–747. DOI: `10.2514/1.19226`. eprint: `https://doi.org/10.2514/1.19226`. URL: `https://doi.org/10.2514/1.19226` (cit. on p. 32).

[27] Christian Cazaux, Firouz Naderi, Charles Whetsel, Dave Beaty, Bob Gershman, Richard Kornfeld, Bob Mitcheltree, and Bob Sackheim. «The NASA/CNES Mars sample return— a status report». In: *Acta Astronautica* 54.8 (2004), pp. 601–617. ISSN: 0094-5765. DOI: `https://doi.org/10.1016/j.actaastro.2003.07.001`. URL: `https://www.sciencedirect.com/science/article/pii/S0094576503002340` (cit. on p. 36).

[28] Mengzhe Li, Chunbo Hu, Zhiqin Wang, Yue Li, Jiaming Hu, Xu Hu, and Chao Li. «Application and performance estimation of Mg/CO2 engine on Mars». In: *Acta Astronautica* 192 (2022), pp. 314–327. ISSN: 0094-5765. DOI: `https://doi.org/10.1016/j.actaastro.2021.12.032`. URL: `https://www.sciencedirect.com/science/article/pii/S0094576521006676` (cit. on p. 37).

[29] William J. O'Neil and Christian Cazaux. «The mars sample return project». In: *Acta Astronautica* 47.2 (2000). Space an Integral Part of the Information Age, pp. 453–465. ISSN: 0094-5765. DOI: `https://doi.org/10.1016/S0094-5765(00)00085-0`. URL: `https://www.sciencedirect.com/science/article/pii/S0094576500000850` (cit. on p. 45).

[30] Norbert Grunwald, Joshua Taron, Olaf Kolditz, R. Liedl, and Chan-Hee Park. «Comparison of equations of state for carbon dioxide for numerical simulations». In: *IAHS-AISH Publication* 355 (Jan. 2012), pp. 252–260 (cit. on p. 49).

[31] Evgeny Shafirovich, Michaël Salomon, and Iskender Gökalp. «Mars hopper versus Mars rover». In: *Acta Astronautica* 59.8 (2006). Selected Proceedings of the Fifth IAA International Conference on Low Cost Planetary Missions, pp. 710–716. ISSN: 0094-5765. DOI: `https://doi.org/10.1016/j.actaastro.`

2005.07.018. URL: `https://www.sciencedirect.com/science/article/pii/S0094576505002237` (cit. on pp. 70, 72).

[32] United States. National Aeronautics and Space Administration. *NASA technical note D-281.* 1960. URL: `https://books.google.it/books?id=1hgjAAAAMAAJ` (cit. on p. 72).